

# Fluid-to-solid transition of hard regular polygons

Joshua A. Anderson,<sup>1</sup> James Antonaglia,<sup>2</sup> Jaime A. Millan,<sup>3</sup> Michael Engel,<sup>1,4</sup> and Sharon C. Glotzer<sup>1,2,3,\*</sup>

<sup>1</sup>*Department of Chemical Engineering, University of Michigan, Ann Arbor, MI 48109, USA*

<sup>2</sup>*Department of Physics, University of Michigan, Ann Arbor, MI 48109, USA*

<sup>3</sup>*Department of Materials Science and Engineering,  
University of Michigan, Ann Arbor, MI 48109, USA*

<sup>4</sup>*Institute for Multiscale Simulation, Friedrich-Alexander-Universität Erlangen-Nürnberg, 91058 Erlangen, Germany*

Characterizing the fluid-to-solid transition (conversely the melting transition) of two-dimensional systems is a fundamental problem in condensed matter physics that has advanced significantly through the application of computational resources and algorithms. Here we report a comprehensive simulation study of the phase behavior near the melting transition of all hard regular polygons with  $3 \leq n \leq 14$  vertices using massively parallel Monte Carlo simulations of up to one million particles. We find that regular polygons with seven or more edges behave like hard disks and melt continuously from a solid to a hexatic fluid and then undergo a first-order transition from the hexatic phase to the fluid phase. Strong directional entropic forces align polygons with fewer than seven edges and improve local ordering in the fluid. These forces can enhance or suppress the discontinuous character of the transition depending on whether the local order in the fluid is compatible with the local order in the solid. Triangles, squares, and hexagons exhibit a KTHNY-type continuous transition between fluid and hexatic, tetratic, and hexatic phases, respectively, and a continuous transition from the appropriate x-atic to the solid. In contrast, pentagons and plane-filling 4-fold pentilles display a one-step first-order melting of the solid to the fluid with no intermediate phase. The thirteen studied systems thus comprise examples of three distinct two-dimensional melting scenarios.

## I. INTRODUCTION

In two-dimensional systems there are three scenarios for fluids to order into equilibrium solids or, equivalently, for solids to melt into fluids [1, 2]. One, the system can exhibit a first-order fluid-to-solid transition. This scenario is almost exclusively found in three dimensions. Systems of hard spheres [3] and hard polyhedra [4] show such a transition. Two, the system can exhibit a continuous fluid-to-x-atic-to-solid transition. Here, the term x-atic refers to an intermediate fluid phase that has quasi-long-range (power-law decay) correlations in the bond order but only short-range (exponential decay) positional order. The hexatic phase, with six-fold bond order, is the most well-known example. The existence of continuous fluid-to-solid transitions was predicted by the Kosterlitz-Thouless-Halperin-Nelson-Young (KTHNY) theory [5–7] and has been confirmed in experiments with paramagnetic colloids [8]. Three, the system can exhibit a first-order fluid-to-x-atic and subsequent continuous x-atic-to-solid transition. This combination of transitions is intermediate to the first-order fluid-to-solid behavior and the KTHNY behavior. It has been observed in simulations of hard disks in two dimensions [9, 10] and under quasi-two-dimensional confinement of hard spheres where out-of-plane fluctuations are limited [11]. Here we test that notion in simulations of hard polygons.

Already small perturbations of the system conditions can change the character of the two-dimensional fluid-to-solid transition. Widening the quasi-two-dimensional

confinement beyond 1.5 sphere diameters [11, 12] or pinning more than 0.4% of the disks on a lattice [13] modifies the transition to one-step first-order. Pinning particles at random positions [14] or softening the interaction potential has the opposite effect and leads to the recovery of the KTHNY scenario. Disks interacting via soft  $r^{-n}$  potentials melt like hard disks for  $n \geq 6$ , but switch to a continuous transition when  $n < 6$  [15]. A hexatic phase is also reported in the system of parallel (*i.e.* non-rotating) hard cubes [16–19]. Upon rounding the cube edges, the transition eventually becomes first-order [20]. A general observation from these examples is that systems in which neighboring particle motions couple stronger (for example due to the presence of interactions) show a more pronounced KTHNY behavior, while weaker coupling (for example in higher dimensions) moves the system towards a first-order fluid-to-solid transition.

Hard polygons have a rotational degree of freedom, which opens the possibility for more complex entropic forces and more diverse solid phases than observed for hard disks. In addition, polygons can exhibit rotator phases in which both the bond order and positional order are quasi-long-ranged, but the particles rotate around their centers of mass. In particular, regular polygons may exhibit a range of fluid-to-solid transition scenarios depending on the degree of faceting of the polygon. Indeed, simulations of equilateral triangles using an approximate event-driven molecular dynamics method showed a continuous fluid-to-liquid crystal-like phase transition [21]. Monte Carlo simulations revisiting that system reported a fluid-to-hexatic transition at  $\phi = 0.70$  and a hexatic-to-solid transition at  $\phi = 0.87$  [22]. Although no experiments have yet been reported on hard, mathematically regular triangles, rounded triangular colloidal platelets

\* [sglotzer@umich.edu](mailto:sglotzer@umich.edu)

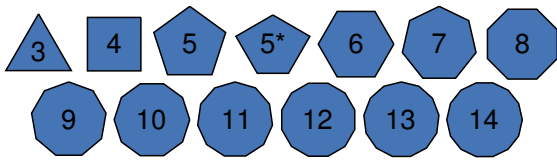


FIG. 1. The polygons studied in this work are the regular  $n$ -gons with  $3 \leq n \leq 14$  and the 4-fold pentille labelled  $5^*$ .

exhibit a fluid-to-hexatic transition [23]. Monte Carlo simulations of squares show a continuous fluid-to-tetratic transition at  $\phi = 0.7$  [24]. Experiments on vibrated granular squares (LEGOs) find tetratic orientational order in the range  $\phi = 0.70$  to  $0.74$  [25]. Tetratic order is also observed in the hard rectangle system [26]. Rounded squares have hexagonal rotator and rhombic crystal phases [27, 28]. Pentagons exhibit a fluid-to-hexagonal rotator transition at  $\phi = 0.68$  [29]. The same rotator phase transition has also been reported with rounded colloidal pentagons at  $\phi = 0.66$  [30]. The data in that work is suggestive of a possible hexatic phase, but is inconclusive due to small system sizes within the field of view of the camera. Pentagon phase behavior has also been studied in systems of 5-fold symmetric molecules [31] and with vibrating shaking tables [32, 33].

A common limitation of all previous studies of hard polygon phase behavior is the relatively small sample sizes of at most a few thousand particles. This makes the full characterization of the fluid-to-solid transition and thus the determination of the presence or absence of x-atic phases difficult. We know from recent hard disk simulations [9, 10] that system sizes of up to a million particles may be needed to sample the long-range correlations and conclusively identify hexatic phases. For this reason, and to serve as reference systems for future two-dimensional simulations, here we determine to high precision the equations of state for all hard regular polygons with  $n \leq 14$  vertices. The data obtained from massively parallel Monte Carlo simulations of up to  $1024^2$  particles allows us to resolve the nature of the fluid-to-solid phase transition in all cases and to analyze the change in phase behavior as particle symmetry decreases.

## II. METHODS

We investigate systems of  $N$  identical polygons with  $n$  edges that interact solely through excluded volume interactions in a box of area  $A_{\text{box}}$ . Particle  $a$  has position  $\vec{r}_a$  and orientation angle  $\theta_a$ . The circumcircle diameter of the polygons is denoted as  $\sigma$ . The majority of our work focuses on regular polygons ( $n$ -gons) with the area of a single particle  $A = \sigma^2 n / 2 \sin(2\pi/n)$ . But we also include the 4-fold pentille [34] in our study, which is the Voronoi cell of the Cairo pentagon pattern and thus tiles space. All thirteen polygons are shown in Figure 1.

## A. Simulation code and computational resources

We performed hard particle Monte Carlo simulations in the isochoric (constant area) ensemble using the HPMC [35] module of HOOMD-blue [36–38]. HPMC (for Hard Particle Monte Carlo) is a parallel simulation implementation on many CPUs or GPUs using MPI domain decomposition. Each simulation begins with the particles being positioned and oriented randomly in a rectangular simulation box. Simulations are performed for a long enough time to reach and statistically sample thermodynamic equilibrium. In all cases we employ periodic boundary conditions.

This work utilized significant computational resources on XSEDE [39] Stampede (222 thousand SUs), OLCF Eos, OLCF Titan (115 million Titan-core-hours), and the University of Michigan Flux cluster (about 100 thousand GPU hours) that hosts our group’s nodes. We conducted simulations for at least  $3 \cdot 10^8$  attempted trial moves per particle and more if necessary for equilibration with four replicates at every state point to determine error bars in the equations of state. We ran small simulations ( $N \leq 256^2$ ) on CPUs with 1024 particles per CPU core, and larger simulations on GPUs with 16000 particles per GPU. The largest simulations at  $N = 1024^2$  used 64 GPUs in parallel for each run, cover 21 different densities, two replicates, and several polygons at a time in 4000-8000 GPU runs on the Titan cluster for more than 100 hours. One such large simulation can thus contain on the order of  $10^{17}$  individual Monte Carlo polygon update moves. At the largest system sizes we simulate only two replicates and do not compute the equation of state, as the additional sampling needed is too computationally expensive.

## B. Equation of state

We compute the equation of state  $P^*(\phi)$  using volume perturbation techniques [40, 41] to measure pressure in isochoric simulations. We report pressure in reduced units  $P^* = P\sigma^2/k_B T$ . In addition to the system density  $\phi = NA/A_{\text{box}}$ , we determine the averaged local density field on a grid,

$$\Phi(\vec{r}_i) = \frac{A \sum_{a=1}^N H(r_c - |\vec{r}_a - \vec{r}_i|)}{\pi \cdot r_c^2}, \quad (1)$$

where we choose the cut-off  $r_c = 20\sigma$  and  $H$  is the Heaviside step function.

With the fluid density  $\phi_f$  and the density of the solid (or hexatic) phase  $\phi_s$  the latent heat  $L = P\Delta A_{\text{box}}$  of a first-order phase transition is

$$\frac{L}{Nk_B T} = P_c^* \frac{A}{\sigma^2} \left( \frac{1}{\phi_f} - \frac{1}{\phi_s} \right), \quad (2)$$

where  $P_c^*$  is the coexistence pressure estimated by Maxwell construction.

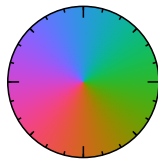


FIG. 2. Cubeellipse color wheel

### C. Order parameters

We use three order parameters that were previously effective at identifying the hexatic phase in the hard disk system [9, 10]. Each order parameter is a complex number on the unit circle.

The positional order parameter

$$\chi^a = e^{i\vec{r}_a \cdot \vec{q}_0} \quad (3)$$

identifies how well the position  $\vec{r}_a$  of particle  $a$  fits on a perfect lattice with reciprocal lattice vector  $\vec{q}_0$ . When all particles have similar phases in  $\chi$ , they are in a solid. Defects cause  $\chi$  to rotate. We choose  $\vec{q}_0$  as the brightest peak in the structure factor [9] computed with the following procedure: (i) Initialize a density grid with roughly  $8 \times 8$  pixels per particle. (ii) At the center of each particle, place a Gaussian on this grid with standard deviation  $\frac{1}{10}\sigma$ . (iii) Take the fast Fourier transform (FFT) of the density grid to get the discretized  $S(\vec{q})$ . (iv) Smooth with a Gaussian filter, standard deviation 2 pixels  $S(\vec{q}) \rightarrow S_{\text{smooth}}(\vec{q})$ . (v) Choose  $\vec{q}_0$  from the location of the brightest pixel in  $S_{\text{smooth}}(\vec{q})$ .

The bond orientation order parameter for  $k$ -fold rotational symmetry

$$\psi_{k,p}^a = \frac{1}{p} \sum_{b \in \text{NN}_p(a)} e^{ik\alpha_{ab}} \quad (4)$$

identifies the orientation of the  $p$  nearest neighbors around particle  $a$ . Here  $\alpha_{ab}$  is the angle the separation vector  $\vec{r}_b - \vec{r}_a$  makes with respect to the positive  $x$ -axis, and  $\text{NN}_p(a)$  is the set of  $p$  nearest neighbors of  $a$ . We omit  $p$  in the subscript when it is equal to  $k$  and write  $\psi_k^a = \psi_{k,k}^a$ . Some authors suggest using a morphometric approach [42] to compute the bond orientation order parameter, which requires computing a Voronoi diagram of the system of particles. We do not adopt this scheme because we find the use of  $p$  fixed neighbors sufficient as it generates order parameter fields fully consistent with the defects present in the system.

The body orientation order parameter

$$\xi_s^a = e^{is\theta_a} \quad (5)$$

identifies the orientation of a particle accounting for  $s$ -fold symmetry. It allows us to analyze the presence of rotator phases in which  $\xi_s^a$  decays to zero rapidly as a function of the separation distance.

### D. Visualization

We visualize order parameter fields directly in the  $x$ - $y$  plane by mapping the argument of the complex values of an order parameter  $v$  to a color wheel. The color wheel is centered by plotting  $\arg(v) - \arg(\langle v \rangle)$ . Short-range order shows up as colors rapidly cycling through the color wheel, quasi-long-range order appears as patches, and long-range order appears as a single solid color green across the box. Two-phase regions show both behaviors in a single simulation box.

The standard hue, saturation, value color wheel introduces visual artifacts, as some colors appear brighter to the eye, and it creates apparent features in the data where there are none. As a perceptually corrected color wheel we use the cubeellipse, which is the color part of the cubehelix [43] color map at constant luminance ( $v = 0.5$ ,  $\gamma = 1$ ,  $s = 4.0$ ,  $r = 1$ ,  $h = 1$ ), shown in Figure 2. The center of this color, and thus the most common color in each image, is green (at the 3 o'clock positions in Figure 2).

In contrast, plots representing non-periodic functions need not be so uniform but instead require a strong contrast between low and high values. We plot the local density field  $\Phi$  with a divergent red-yellow-blue color map with the fluid density mapped to red and the solid density mapped to blue.

### E. Correlation functions

Correlation functions measure the behavior of the order parameters as the separation  $r_{ba} = |\vec{r}_b - \vec{r}_a|$  between a pair of particles increases. The correlation functions for bond orientation order and body orientation order are implemented in our analysis code as

$$C_v(r) = \frac{\sum_{b \in S(m,N)} \sum_{a=1}^N v^a (v^b)^* \delta(r - r_{ba})}{\sum_{b \in S(m,N)} \sum_{a=1}^N \delta(r - r_{ba})}, \quad (6)$$

where  $v = \psi_{k,p}$  or  $\xi_n$  and  $v^*$  is the complex conjugate. The sampling  $S(m, N)$  randomly selects  $m$  particles out of  $N$  without replacement.

One can compute a correlation function from the positional order parameter  $\chi$ , but it is extremely sensitive to the choice of  $\vec{q}_0$ . We observe that peaks misidentified by only a single pixel result in an apparent lack of quasi-long-range positional order. Instead, we follow Ref. [9] and compute positional correlation functions from

$$C_g(r) = \frac{\langle g_\psi((r, 0), \alpha) \rangle - 1}{\max(\langle g_\psi((r, 0), \alpha) \rangle - 1)}, \quad (7)$$

which oscillates, so we show only identified peaks. The signal then decays to about  $10^{-3}$  at large  $r$ . The function  $g_\psi(\vec{r}, \alpha)$  is the discretized two dimensional pair correlation function obtained by correlated averaging over

individual measurements with index  $i$ ,

$$g_\psi(\vec{r}_i, \alpha) = \frac{\sum_{b \in S(m, N)} \sum_{a=1}^N d_\kappa(R(-\alpha)\vec{r}_{ba} - \vec{r}_i)}{m/A}, \quad (8)$$

where  $R(\beta)$  is the rotation matrix that rotates a vector by the angle  $\beta$ ,  $\Delta r$  is the bin size, and  $d_\kappa$  is the coarse-grained delta function

$$d_\kappa(\vec{r}) = \begin{cases} (\Delta r)^{-2} & \text{if } 0 \leq r_x, r_y < \Delta r, \\ 0 & \text{otherwise.} \end{cases} \quad (9)$$

Since the system rotates from frame to frame, it must be aligned to the bond orientation order parameter before averaging. To do this, we compute  $g_\psi(\vec{r}_i, \alpha)$  over many frames with large  $m$ . We align each frame using the bond orientation order parameter averaged over all particles in the frame,  $\alpha = \arg(\langle \psi_{k,p} \rangle)$ . Averaging the separately aligned  $g_\psi(\vec{r}_i, \alpha)$  and then computing  $C_g(r)$  significantly reduces noise [10].

### F. Sub-block scaling analysis

The sub-block scaling of  $\chi$  is a sensitive measure of the density of the hexatic to solid transition [13, 44]. The first density that sits on or under a line of slope  $-1/3$  is at the hexatic to solid transition. Similarly, sub-block scaling in  $\psi$  determines the density at which the hexatic melts into the fluid, with a line of slope  $-1/4$ .

We perform a sub-block scaling analysis on the positional order parameter  $\chi$  and the bond orientational order parameter  $\psi_{k,p}^a$ . For this analysis the simulation box of length  $L$  is divided into squares of side length  $L_b$ . Within each box, we calculate

$$v(L_b) = \left\langle \left| \frac{1}{N} \sum_{a=1}^{N_{L_b}} v^a \right| \right\rangle, \quad (10)$$

where  $v = \psi_{k,p}$  or  $\chi$ ,  $N_{L_b}$  is the number of particles in a sub-block and  $\langle \rangle$  denotes averaging over sub-blocks in the same snapshot. Standard errors are calculated by averaging the values of  $v(L_b)$  over independent frames.

### G. Topological defect analysis via cell-edge counting

We use a Voronoi tessellation of the set of particle centers to count edges of Voronoi cells in the case of the hexagonal solid. This generates statistics of topological defects. Each particle  $a$  is assigned the number of adjacent Voronoi cells  $n_a$  and the disclination charge  $q_a = n_a - 6$ . In the presence of well-separated topological defects, disclinations can be found by identifying particles with non-zero disclination charge, and dislocations correspond to bounds pairs of a five-coordinated particle ( $q = -1$ ) and a seven-coordinated particle ( $q = +1$ ).

However, while disclination charges with  $|q| > 1$  are very rare in our hard particle systems, particles with non-zero disclination charge are often not clearly separated or bound into pairs but instead agglomerate into larger clusters. This makes it ambiguous to identify the locations of individual disclinations and dislocations.

To overcome this ambiguity, we cluster defects if they are in adjacent Voronoi cells and calculate the total disclination charge  $q = \sum q_a$  of the cluster [45]. For disclination-neutral clusters ( $q = 0$ ), the total Burgers vector  $\vec{b}$  around the cluster can be determined from the disclination charges and their positions,

$$\vec{b} = \hat{z} \times \sum_a q_a \vec{r}_a, \quad (11)$$

where  $\hat{z}$  is the unit vector along the  $z$ -axis and the cross product is performed in three-dimensional space. Because Burgers vectors are topologically restricted to be lattice vectors, the vector we obtain from this computation is then snapped to its closest lattice point in a hexagonal lattice whose lattice spacing is that of the ideal lattice at the density of the simulation frame. We count the number of particles in three types of defect clusters, overall neutral ( $q = 0$ ,  $\vec{b} = 0$ ), Burgers-charged ( $q \neq 0$ ,  $\vec{b} \neq 0$ ), and disclination-charged ( $q \neq 0$ ) as a function of density.

## III. RESULTS AND DISCUSSION

The same analysis was performed for each of the thirteen polygons (triangle to 14-gon and 4-fold pentille) investigated in this work. We first discuss general aspects of the data obtained and later focus on details of individual fluid-to-solid transition scenarios. Note that some of the detailed figures were moved to the end of the manuscript to avoid cluttering the manuscript due to their large number. Within the text we only include a few representative plots and snapshots.

### A. Simulation data and analysis

Summary panels for every polygon studied in this work are shown in Figures 9–21. Each panel includes in the top part of the figure the equation of state  $P^*(\phi)$  (top left), the local density histogram (middle left), the sub-block scaling analysis (bottom left), the correlation of the bond orientation  $C_{\psi_{k,p}}(r)$  (top right), the correlation of the body orientation  $C_g(r)$  (middle right), and the positional correlation  $C_{\xi_n}(r)$  (middle bottom). We only compute correlation functions in single-phase regions. Dashed lines guide the eye to show various exponential and power law decay curves.

Simulation snapshot images at evenly spaced densities across the transition region are shown in the bottom part of Figures 9–21. Each image from top to bottom shows

the bond orientation order parameter field  $\psi_{k,p}$ , the positional order parameter field  $\chi$ , the body orientation order parameter field  $\xi_p$ , the local density field  $\Phi$ , and the structure factor  $S(\vec{q})$ . The data is taken from the final frame of the largest simulation performed. Along the bottom, we show the density  $\phi$  of each column and the phase we identify.

## B. Phase determination

We identify first-order transitions using the following criteria: (i) a two-phase region is evident in isochoric simulations, (ii) the two phases have different densities, and (iii) the equation of state has a Mayer-Wood loop [10] in the equation of state, which decreases in height as  $N$  increases. In contrast, continuous transitions have a monotonic equation of state and only a single phase at a single density is present in each frame across the entire transition. The signature of two phase regions includes a bimodal local density histogram along with two different correlation length behaviors seen in the  $\psi$  and  $\chi$  order parameter fields coincident with the low and high local densities. In all cases where we find a Mayer-Wood loop, we observe two-phase regions, and in all cases where we find a continuous equation of state, we observe only single phases across the transition.

Correlation lengths vary significantly in the simulations. In the fluid phase, positional order  $\chi$  decorrelates instantly with correlation lengths of only  $1\sigma$ . Bond orientational order  $\psi_{k,p}$  persists a bit further with correlation lengths of tens of  $\sigma$  but still exhibits clear short-range order. In the hexatic phase,  $\chi$  oscillates visibly through the full color wheel along a given direction forming stripes, a behavior indicative of short-range order. Unbound dislocations exist at the end of each stripe. For continuous phase transitions, the oscillation period gets larger as density increases. Solid phases lead to patchy motifs in  $\chi$  (quasi-long-range order). Two-phase regions show a combination of two of these motifs in a single system.

Our observations confirm in all cases that we have run simulations sufficiently large to allow the fluctuations in the order parameter fields of the fluids and x-atics to occur several times across the box. Only in the solid phase regions are the order parameter fields essentially constant and vary by less than one period.

## C. KTHNY behavior

Our data show that triangles, squares, and hexagons have continuous fluid-to-x-atic and continuous x-atic-to-solid transitions. We refer to the monotonic equation of state in Figure 9, Figure 10, and Figure 13 for the triangle, square, and hexagon data, respectively. Triangles and hexagons have hexatic order with a signal in  $\psi_6$ , and squares have tetratic order with a signal in  $\psi_4$ . Figure 3a–c demonstrates the continuous transitions for

hexagons, with a single density at each state point and gradually developing order in the order parameter fields.

### 1. Decay of correlation functions

The first state point showing quasi-long-range bond orientation order in the hexagon system is  $\phi = 0.686$ . At this density, positional order is extremely short-ranged, persisting for only a few particle diameters. As density increases, the decay length of the positional order becomes longer, up to hundreds of particle diameters at  $\phi = 0.702$ , and begins to diverge. At  $\phi = 0.708$ , positional order switches to quasi-long-range and the system is in the solid phase as determined by sub-block scaling. KTHNY theory predicts a slope of  $-1/4$  in  $\psi_6$  scaling at the fluid to hexatic transition, a perfect match for the  $\phi = 0.686$  line in Figure 3c. The theory also predicts a slope of  $-1/3$  for  $\chi$  scaling, which similarly matches the scaling for  $\phi = 0.708$ . At the same density, the directly computed positional correlation  $C_g(r)$  length is beginning to diverge so it is difficult to determine the exact density of the hexatic to solid transition from correlation functions alone.

### 2. Topological defects and local order

The KTHNY melting scenario is two-step. Dislocations unbind to drive the transition from solid to hexatic, and then disclinations unbind to drive the transition from hexatic to fluid. The KTHNY theory provides a picture of tightly bound defects transitioning to free defects in both melting steps. However, both Bernard *et al.* [9] and this work show that defects are not free, but rather form large and complex clusters, often highly anisotropic, indicating medium-ranged effective inter-defect interactions. In the extreme case that defects cluster into one-dimensional strings, such a scenario would lead to grain-boundary induced melting [46, 47].

We employ cell-edge counting to determine the number of defect particles that comprise clusters of defects that are overall neutral, those with a Burgers charge, and those with disclination charge. We examine these counts as a function of density. A large number of free dislocation clusters with non-zero Burgers vectors simultaneous with few free disclinations is evidence for the hexatic phase. Figure 4c shows this behavior. The count of particles in Burgers-charged clusters begins increasing just below  $\phi = 0.710$  at the solid to hexatic transition. The count of particles in disclination-charged clusters remains low, and starts ramping up slowly in the middle of the hexatic phase at  $\phi = 0.696$ . Throughout the hexatic phase, we find many more particles in Burgers-charged clusters than in disclination-charged clusters. This is consistent with the two-step KTHNY melting scenario and the continuous phase transitions we observe for hexagons.

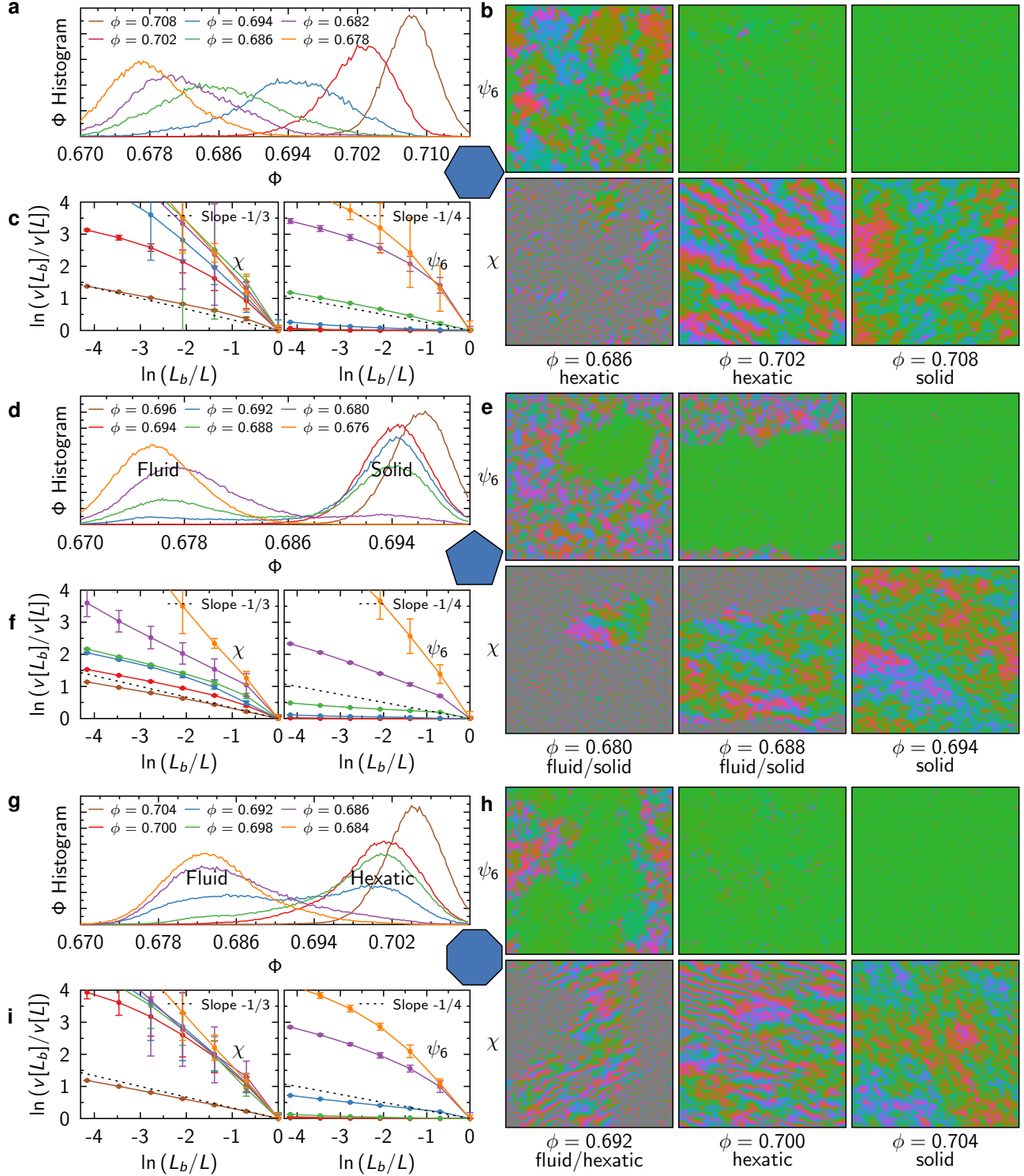


FIG. 3. Example phase transitions from the three melting scenarios. We show data for (a-c) hexagons ( $N = 512^2$ ) following the KTHNY scenario, (d-f) pentagons ( $N = 1024^2$ ) exhibiting a first-order fluid-to-solid transition, and (g-i) octagons ( $N = 1024^2$ ) following an intermediate scenario exhibiting a first-order fluid-to-hexatic transition. For each shape, the top left panels show local density histograms (a,d,g). The right panels show bond and positional order parameters at selected densities (b,e,h). The bottom left panels show sub-block scaling analysis (c,f,i).

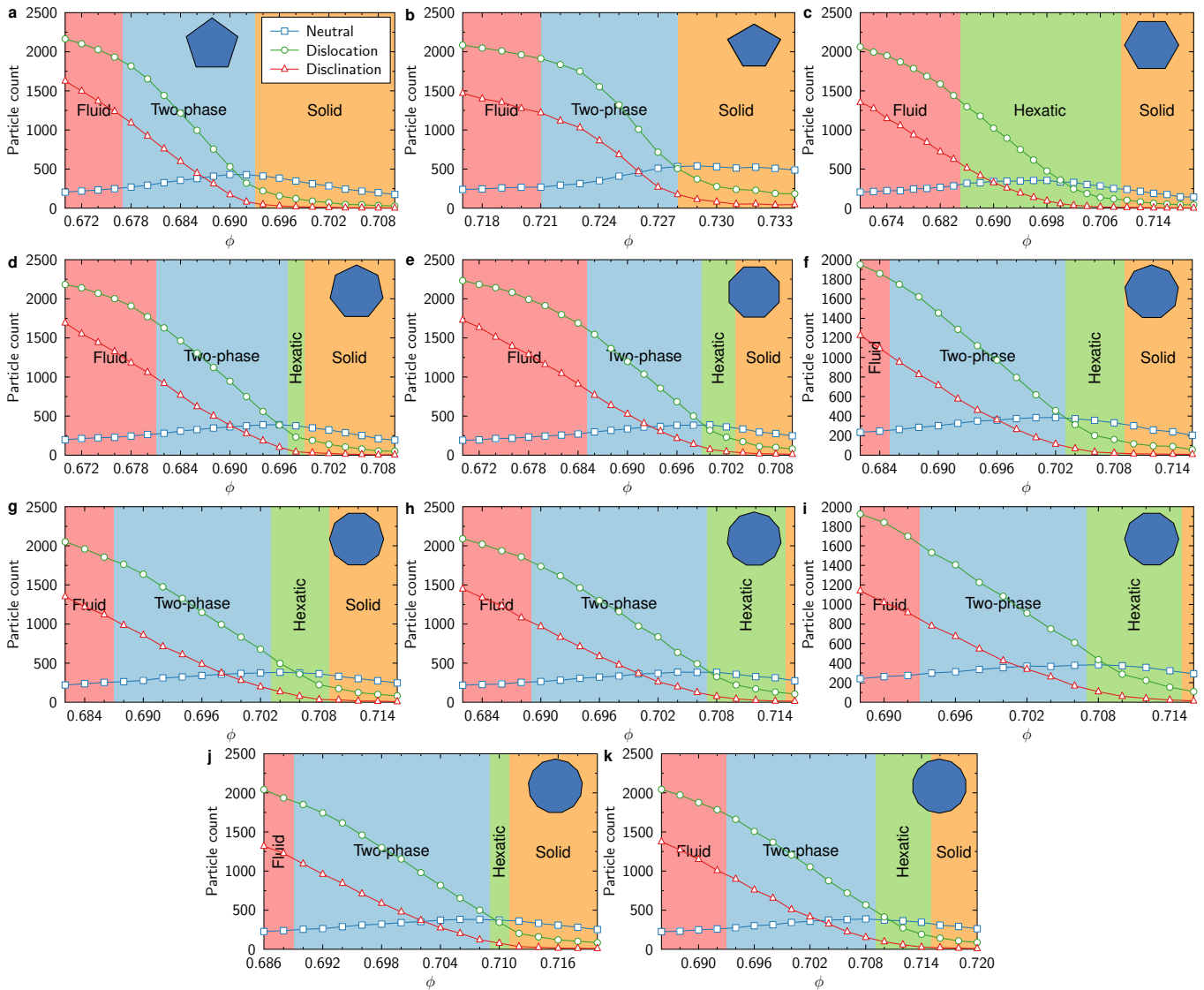


FIG. 4. Defect counts as a function of density obtained with cell-edge counting. The particle count is the number of particles that belong to any defect cluster classified into neutral, Burgers-charged and disclination-charged clusters. The figures show results of the defect analysis plots for polygons  $n = 5, 6, 7, 8, 12$ , averaged over 4–8 runs with 19–49 frames per run at the system size  $N = 128^2$ . The defect count algorithm is expensive, so we do not run it on the largest size simulations we performed. We also show the phase diagram overlaid on the counts. Error bars at one standard deviation are smaller than the symbol size.

Figure 5a shows the structure of the defects in a system of hexagons at  $\phi = 0.690$ , in the hexatic phase. The density of free dislocations (red and green pairs) is much higher than that of free disclinations (there is a single lone green particle in the image), but the structure is more complicated because the defects combine into large clusters. The left panel of Supplementary Movie 1 shows how defects migrate as the Monte Carlo simulation progresses via local moves for a simulation of hexagons at  $\phi = 0.690$ . Dislocations are unstable and highly mobile, quickly hopping between sites and popping in and out of existence. We find that the count of nearest neighbors is very sensitive to small changes in particle coordinates.

We also compute the isoperimetric quotient  $IQ =$

$4\pi A/P^2$  for each Voronoi cell, where  $A$  is the area and  $P$  is the perimeter of the cell. Regular polygons have the value  $IQ = \pi/(n \tan(\pi/n))$ . More elongated Voronoi cells have low  $IQ$  and indicate locations of large crystal deformity, which makes  $IQ$  an approximate indicator of defects. Figure 5b and the right panel of Supplementary Movie 1 color particles by  $\langle IQ \rangle - IQ$ . Blue indicates large deviation from  $\langle IQ \rangle$  and yellow indicates little deviation. If  $IQ > \langle IQ \rangle$ , the particle is darkened, as these particles are closest to having regular crystal environments.

The coloring scheme based on the isoperimetric quotient  $IQ$  is a continuous quantity and, as seen in the movie, is less sensitive to small particle displacements. In contrast, the number of edges of a Voronoi cell changes

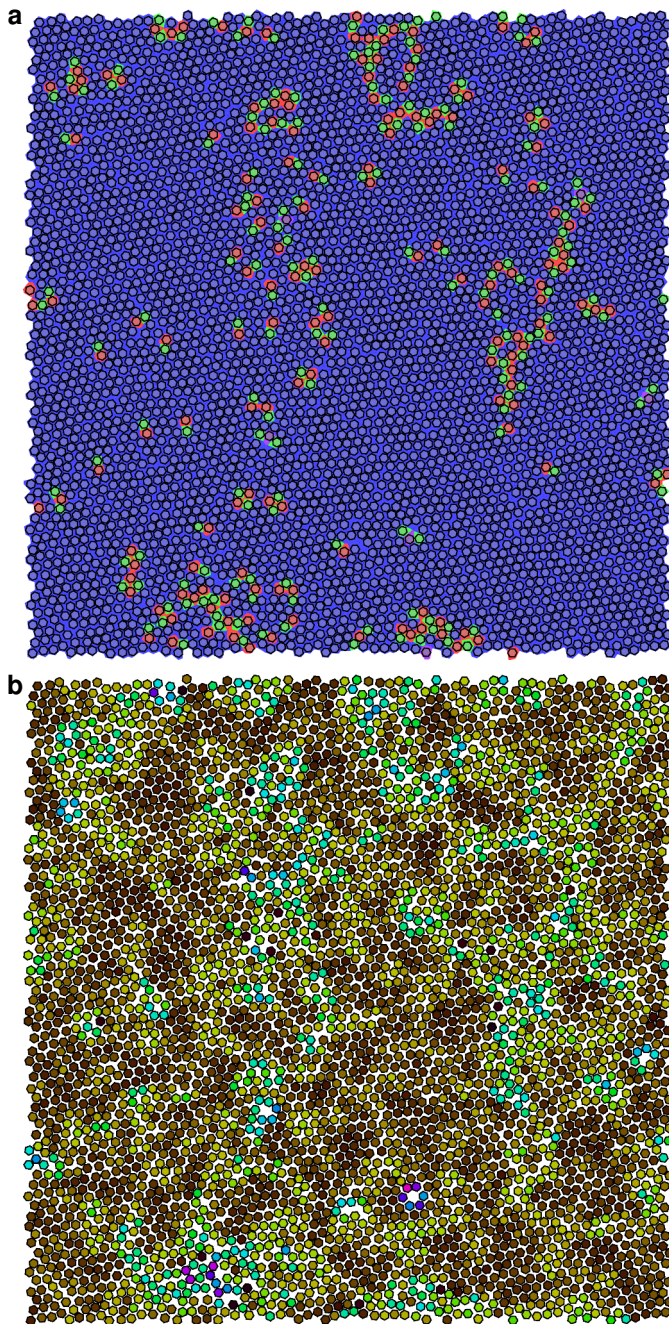


FIG. 5. Representative snapshot of the hexagon system  $N = 128^2$  at density  $\phi = 0.690$ . (a) Particles are colored by the number of edges in the Voronoi cell. Red, blue, and green cells have seven, six, and five sides respectively. (b) Particles are colored by  $\langle IQ \rangle - IQ$ . Blue indicates large deviation from  $\langle IQ \rangle$  and yellow indicates little deviation.

discontinuously across Monte Carlo steps. This suggests  $\langle IQ \rangle - IQ$  might be a more robust indicator of defect concentrations on short time scales, while cell-edge counting is simple and reliable for long time averages over uncorrelated frames. We also note that in systems of triangles and squares defects are even more delocalized and

Polygon	Cross-correlation	Phase		
		Fluid	x-atic	Solid
Triangle	$ \langle \psi_{6,3} \xi_6^* \rangle $	0.117	0.221	0.236
Square	$ \langle \psi_4 \xi_4^* \rangle $	0.449	0.790	0.810
Pentagon	$ \langle \psi_6 \xi_{10}^* \rangle $	0.001	-	0.001
Hexagon	$ \langle \psi_6 \xi_6^* \rangle $	0.244	0.294	0.299
Heptagon	$ \langle \psi_6 \xi_{14}^* \rangle $	0.001	0.001	0.001
Octagon	$ \langle \psi_6 \xi_8^* \rangle $	0.001	0.001	0.001
Dodecagon	$ \langle \psi_6 \xi_{12}^* \rangle $	0.001	0.039	0.039

TABLE I. Cross-correlation between bond and body orientation in the fluid, x-atic, and solid phases. We select the highest density pure fluid phase, the highest density pure x-atic phase, and the lowest density pure solid phase. Errors of two standard deviations of the mean are approximately 0.001 for all values.

Voronoi cell-edge counting is unable to identify defects, while  $\langle IQ \rangle - IQ$  can still identify areas where defects are present.

### 3. Particle alignment

At all densities we simulate for triangles, squares, and hexagons, the body order parameter  $\xi_s$  closely matches that of the bond order parameter  $\psi_{k,p}$ . We quantify this by computing the cross-correlation between the two quantities  $|\langle \psi_{k,p} \xi_s^* \rangle|$  in the fluid, hexatic, and solid phases (Table I). We expect high bond-body cross-correlation at high density when particle rotation becomes locked in, as found in previous studies [29]. However, a strong signal is present even in the fluid for triangles, squares, and hexagons.

The cross-correlation results demonstrate alignment of the edges of neighboring particles. This can be interpreted as an effect of directional entropic forces [48]. We quantify the alignment with the potential of mean force and torque (PMFT) [49], computed from runs in the highest density pure fluid phase for each polygon. For each particle, we determine the relative position of its neighbors and construct histograms using many frames to obtain reliable averages. The free energy  $F$  of a given configuration is related to the negative logarithm of the histogram. We average an area in the PMFT  $25\sigma$  from the center to set  $F = 0$  as a baseline.

Figure 6 shows the results of this calculation. All low-symmetry regular polygons ( $n \geq 7$ ) have distinctly separated wells for edge-to-edge contacts at  $F = -1.5k_B T$ . This indicates preferential edge-to-edge alignment in the solid by strong directional entropic forces. But only when the symmetry of the particle shape is compatible with the symmetry of the bond order, as found in hexagons, triangles, and squares, does such edge-to-edge alignment promote local solid motifs in the fluid. Such a pre-ordered fluid allows the correlation length to increase smoothly from short-range to quasi-long-range and the transition

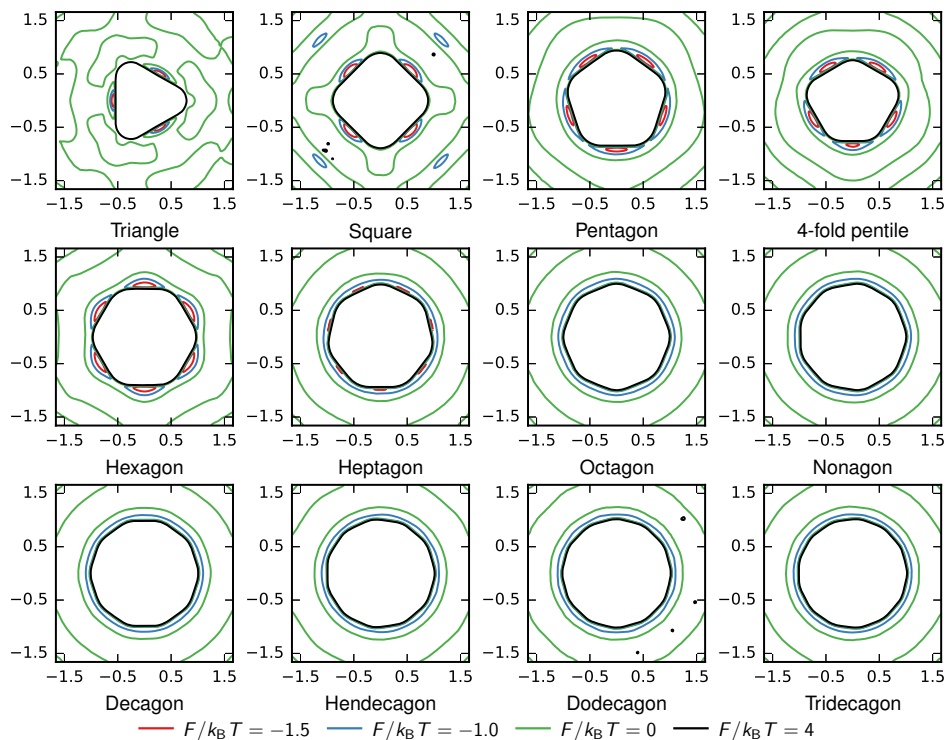


FIG. 6. Potential of mean force and torque plots for polygons  $n=3-13$  computed at the highest density fluid for each polygon. We choose the zero energy reference as the average over a large region  $25\sigma$  from the center (not shown). The data is shown as a contour plot with selected free energy or entropy well contours. Computed from  $N = 256^2$  simulations.

to the solid to be continuous.

Triangles and squares have a distinct overall behavior from hexagons due to the delocalized defects. They have a smeared out phase transition between  $\phi = 0.71$  and  $\phi \approx 0.8$  (Figure 7). Their equations of state are smooth and slowly increasing with barely detectable kinks (Figure 9 and Figure 10). In comparison, the hexagon equation of state has sharp kinks and almost levels off through the transition (Figure 13). Interestingly the melting transition of hexagons becomes more continuous as the system size increases and could, in fact, be mistaken for a first order transition in small systems of only a few thousand particles.

#### D. First-order fluid-to-solid

The regular pentagon has a first-order transition directly from the fluid to the solid. This is seen in Figure 3d-f at  $\phi = 0.688$ . There is a stripe of low density ( $\Phi = 0.676$ ) next to a stripe of solid ( $\Phi = 0.694$ ) with quasi-long-range positional order. The two phase region starts at  $\phi = 0.680$  and the pure solid phase starts at  $\phi = 0.694$ . The two phase region is coincident with a Mayer-Wood loop in the equation of state (Figure 11). The symmetry of the pentagon is not compatible with hexagonal ordering in the solid, so even though it has strong edge-edge bonds, the body-bond

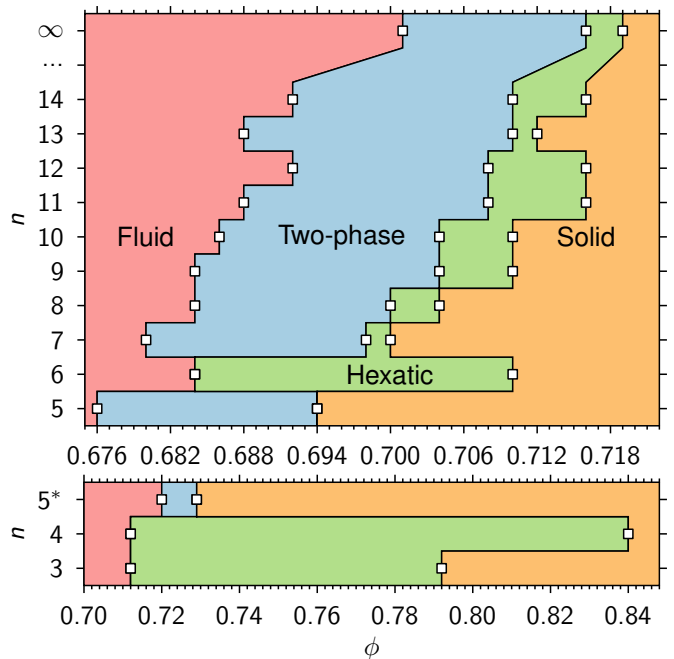


FIG. 7. Phase diagram of hard polygon melting behavior. Disk results ( $n \rightarrow \infty$ ) are from [9, 10]. The label 5\* refers to the 4-fold pentile.

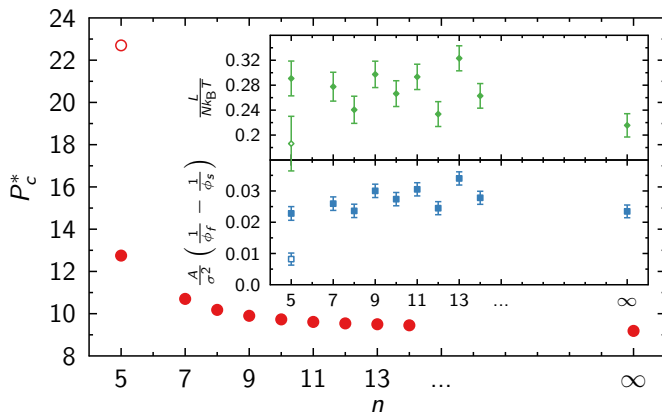


FIG. 8. Latent heat (green diamonds) of the first-order phase transition and the two component factors plotted separately.  $P_c^*$  (red circles) is the coexistence pressure and the area difference per particle  $\delta A$  is shown below (blue squares). Filled symbols are regular polygons, and the open symbols are the 4-fold pentille. Error bars are estimated at 0.001 error in the transition densities. Data for disks ( $n \rightarrow \infty$ ) is from [9].

cross-correlation (Table I) is zero and the phase transition becomes first-order.

The one-step melting process of pentagons also shows up in the defect counts Figure 4a,b. We observe sharp kinks just below the pure solid phase at  $\phi = 0.692$  for counts in clusters with Burgers and disclination charges. One-step melting is supported by this coincident increase in the number of free dislocations and free disclinations.

Of all the regular shapes we studied, only triangles, squares, and hexagons fill space. These are also the only three KTHNY-type shapes. To test if another space filling polygon behaves similarly, we conducted simulations of the 4-fold pentille [34], an irregular pentagon with two different edge lengths that tiles space with 4-fold symmetry. We find that the 4-fold pentille behaves like the regular pentagon, with a first-order fluid-to-solid transition and no intermediate hexatic, though the transition occurs at a higher pressure (Figure 12). At high fluid densities, directional entropic forces (Figure 6) are blurred by the edge lengths and the resulting ten-fold particle body order is not compatible with either the tiling or the hexagonal solid motifs, so the transition is first-order. This suggests the space-filling property itself is not the factor triggering KTHNY melting but instead the similarity between the local order in the dense fluid and the local order in the solid.

### E. Disk-like behavior

Figure 7 summarizes the phases found for all regular polygons studied in this work and includes the hard disk phase diagram ( $n \rightarrow \infty$ ) for comparison. Disks have a first-order fluid-to-hexatic transition, a narrow region of stability for the hexatic phase, and a continuous hexatic-

to-solid transition. A similar smooth behavior with  $n$  is found in the latent heat of the first-order transitions (Figure 8). The coexistence pressure decreasing monotonically as  $n$  increases, approaching that of disks. The 4-fold pentille is an outlier compared to the regular polygons with almost a factor of two higher coexistence pressure.

We executed simulations up to  $n = 14$  in this work and find that all regular polygons with  $n \geq 7$  have first-order fluid-to-hexatic and continuous hexatic-to-solid phase transitions. Figure 3g-i illustrates this for the octagon. In the two-phase region we see a mixture of fluid and hexatic phases. This is the same behavior as seen for disks, the only difference is that the transition shifts to lower packing fraction as  $n$  decreases. At  $n = 7$  the start of the phase transition is at  $\phi = 0.680$ , increases to  $\phi = 0.692$  by  $n = 12, 14$  then again increases to  $\phi = 0.702$  for disks. We observe a small jump in critical density from  $n = 14$  to disks, despite the very close coexistence pressures. We surmise that all regular polygons with  $n \geq 7$  have a first-order fluid-to-hexatic transition followed by a continuous hexatic-to-solid transition, with the transition range shifting higher in density with larger  $n$ .

Of the studied polygons with  $n \geq 7$ , only the dodecagon with  $n = 12$  has a particle symmetry compatible with the bond order in the solid. Although for this polygon strong directional entropic forces have the potential to drive a continuous transition from the fluid to the hexatic and solid phase, the simulations show a clear first-order transition for dodecagons. There is no body-bond cross-correlation in the fluid (Table I), but it does appear weakly in the hexatic phase. The relatively short edge lengths in the dodecagon lower the strength of edge-edge alignment to the point where it is not strong enough to encourage local hexagonal motifs in the fluid, and the transition from bond orientation disorder to order becomes sharp. All regular polygons with  $n \geq 7$  have smeared out  $F = -1k_B T$  contact wells (Figure 6) that encircle the polygon, indicating weaker edge-edge alignment than triangles, squares, and hexagons, allowing a much more isotropic behavior. This is why all regular polygons  $n \geq 7$  share the same fluid-solid transition properties as disks.

Regular polygons with  $n \geq 7$  exhibit an intermediate hexatic phase with a very narrow region of stability and a first-order transition to the fluid. As a result, the defect counts (Figure 4d-k) for these polygons is not as clear. The Burgers-charged and disclination-charged counts for these polygons have sharper kinks than the hexagons, but they do not parallel each other as closely as in the pentagons. Despite this, the hexatic-to-solid transition follows KTHNY predictions. In particular, the sub-block scaling analysis for  $\chi$  predicts the hexatic-to-solid transition density with high accuracy, as shown in Figure 3i where the scaling line for  $\phi = 0.704$  falls almost exactly on the dotted line predicted by theory.

## IV. CONCLUSION

In 1988, Strandburg wrote [1]: “For a decade now the nature of the two-dimensional melting transition has remained controversial.” At that time at least three fluid-to-solid transition scenarios were considered, but in many cases the available evidence was inconclusive as to which system shows which scenario and whether all scenarios indeed occur. Two-dimensional simulations have come a long way since 1988. With the advancement of high-performance computing we can now obtain correlation functions with high enough precision and rely on additional analysis techniques like order parameter fields, sub-block scaling, and cell-edge counting. Together, these tools reliably identify hexatic phases and resolve the nature of the two-dimensional melting transition. Today, we can safely say that the three scenarios discussed already 30 years ago indeed occur and, in fact, can be observed in a single system, the hard polygon systems studied in the present work.

As we have demonstrated, the degree of edge-faceting of polygons and the compatibility of their shape with the lattice of the solid phase together determine the melting scenario. Triangles, squares, and hexagons follow the KTHNY scenario well. They have long edges and strong directional forces that preorder the fluid into symmetries that are compatible with the solid. Pentagons and plane-filling 4-fold pentilles have similar aligning forces in the fluid, but their symmetry is incompatible with hexagonal order. As a result they display a clear one-step first-order melting of the solid to the fluid with no intermediate phase. Regular polygons with sufficiently many ( $n \geq 7$ ) edges have no preferential alignment. They show a close resemblance to hard disk behavior and exhibit a first order fluid-to-hexatic phase transition, the intermediate scenario between KTHNY and one-step first-order melting.

The techniques used in this work demonstrate a decrease first of the number of disclination-charged clusters and later of the number of Burgers-charged clusters as the fluid moves through the hexatic (when it exists) to the solid phase. But we did not yet identify the geometric shape of defect clusters and their interaction, or the free energy cost for creating defects. Further improving the characterization of topological defect clusters would be helpful. A more sophisticated analysis of particles’ kinetics and medium-scale structure, not necessarily larger simulation sizes, could further clarify why systems of two-dimensional polygons melt the way they do in our simulations.

## V. ACKNOWLEDGMENTS

This work was supported by the National Science Foundation, Division of Materials Research Award #DMR 1409620 (to J.A.A. and S.C.G.), US Army Research Office Grant W911NF-10-1-0518 (to S.C.G. and M.E.), National Science Foundation Graduate Research Fellowship Grant DGE 1256260 (to J.A.), and the DOD/ASD(R&E) under Award No. N00244-09-1-0062. Any opinions, findings, and conclusions or recommendations expressed in this publication are those of the authors and do not necessarily reflect the views of the DOD/ASD(R&E). M.E. acknowledges funding by Deutsche Forschungsgemeinschaft through the Cluster of Excellence Engineering of Advanced Materials.

All data analysis in this work was performed using Freud, an in-house Python-driven high-performance toolkit developed by the Glotzer Group. Matthew Spellings implemented the complex correlation function routine and the cubeellipse color map. Eric S. Harper implemented the PMFT analysis code and parallelized all modules. We thank Wenbo Shen for suggesting that we examine correlations in the body orientation order parameter, and Greg van Anders for a critical read of the manuscript.

This work used resources of the Oak Ridge Leadership Computing Facility at the Oak Ridge National Laboratory, which is supported by the Office of Science of the U.S. Department of Energy under Contract No. DE-AC05-00OR22725, on the Extreme Science and Engineering Discovery Environment (XSEDE), which is supported by National Science Foundation grant number ACI-1053575, and also on computational resources and services provided by Advanced Research Computing Technology Services at the University of Michigan, Ann Arbor.

## VI. AUTHOR CONTRIBUTIONS

J. A. Anderson ran the large scale simulations and analyzed the data. J. Antonaglia analyzed the defects. J. A. Millan executed small scale simulations and determined regions of interest. J. A. Anderson and M. Engel conceived the project. S. C. Glotzer supervised the research. All authors discussed methods and results and participated in writing the manuscript.

[1] K. J. Strandburg, *Reviews of Modern Physics* **60**, 161 (1988).

[2] D. R. Nelson, *Defects and Geometry in Condensed Matter Physics* (Cambridge University Press, 2002).

[3] B. J. Alder and T. E. Wainwright, *Journal of Chemical Physics* **27**, 1208 (1957).

[4] P. F. Damasceno, M. Engel, and S. C. Glotzer, *Science* **337**, 453 (2012).

- [5] J. M. Kosterlitz and D. J. Thouless, *Journal of Physics C: Solid State Physics* **6**, 1181 (1973).
- [6] B. I. Halperin and D. R. Nelson, *Physical Review Letters* **41**, 121 (1978).
- [7] A. P. Young, *Physical Review B* **19**, 1855 (1979).
- [8] K. Zahn, R. Lenke, and G. Maret, *Physical Review Letters* **82**, 2721 (1999).
- [9] E. P. Bernard and W. Krauth, *Physical Review Letters* **107**, 155704 (2011).
- [10] M. Engel, J. A. Anderson, S. C. Glotzer, M. Isobe, E. P. Bernard, and W. Krauth, *Physical Review E* **87**, 042134 (2013).
- [11] W. Qi, A. P. Gantapara, and M. Dijkstra, *Soft Matter* **10**, 5449 (2014).
- [12] M. Schmidt and H. Löwen, *Physical Review E* **55**, 7228 (1997).
- [13] W. Qi and M. Dijkstra, *Soft Matter* **11**, 2852 (2015).
- [14] S. Deuschländer, T. Horn, H. Löwen, G. Maret, and P. Keim, *Physical Review Letters* **111**, 1 (2013).
- [15] S. C. Kapfer and W. Krauth, *Physical Review Letters* **114**, 35702 (2015).
- [16] J. A. Cuesta, *Physical Review Letters* **76**, 3742 (1996).
- [17] E. Jagla, *Physical Review E* **58**, 4701 (1998).
- [18] B. Groh and B. Mulder, *Journal of Chemical Physics* **114**, 3653 (2001).
- [19] W. G. Hoover, C. G. Hoover, and M. N. Bannerman, *Journal of Statistical Physics* **136**, 715 (2009).
- [20] M. Marechal, U. Zimmermann, and H. Löwen, *Journal of Chemical Physics* **136**, 144506 (2012).
- [21] M. Benedict and J. Maguire, *Physical Review B* **70**, 174112 (2004).
- [22] A. P. Gantapara, W. Qi, and M. Dijkstra, *Soft Matter* **11**, 8684 (2015).
- [23] K. Zhao, R. Bruinsma, and T. G. Mason, *Nature Communications* **3**, 801 (2012).
- [24] K. W. Wojciechowski and D. Frenkel, *Computational Methods in Science and Technology* **10**, 235 (2004).
- [25] L. Walsh and N. Menon, preprint arXiv:1510.00656.
- [26] A. Donev, J. Burton, F. H. Stillinger, and S. Torquato, *Physical Review B* **73**, 054109 (2006).
- [27] K. Zhao, R. Bruinsma, and T. G. Mason, *Proceedings of the National Academy of Sciences* **108**, 2684 (2011).
- [28] C. Avendaño and F. A. Escobedo, *Soft Matter* **8**, 4675 (2012).
- [29] T. Schilling, S. Pronk, B. Mulder, and D. Frenkel, *Physical Review E* **71**, 036138 (2005).
- [30] K. Zhao and T. G. Mason, *Physical Review Letters* **103**, 13 (2009).
- [31] T. Bauert, L. Merz, D. Bandera, M. Parschau, J. S. Siegel, and K.-H. Ernst, *Journal of the American Chemical Society* **131**, 3460 (2009).
- [32] Y. L. Duparcmeur, A. Gervois, and J. P. Troadec, *Journal of Physics: Condensed Matter* **7**, 3421 (1995).
- [33] S. Sachdev and D. R. Nelson, *Physical Review B* **32**, 1480 (1985).
- [34] J. H. Conway, H. Burgiel, and C. Goodman-Strauss, *The Symmetries of Things* (A K Peters/CRC Press, 2008).
- [35] J. A. Anderson, M. Eric Irrgang, and S. C. Glotzer, *Computer Physics Communications* **204**, 21 (2016).
- [36] J. A. Anderson, C. D. Lorenz, and A. Travasset, *Journal of Computational Physics* **227**, 5342 (2008).
- [37] J. Glaser, T. D. Nguyen, J. A. Anderson, P. Lui, F. Spiga, J. A. Millan, D. C. Morse, and S. C. Glotzer, *Computer Physics Communications* **192**, 97 (2015).
- [38] “HOOMD-blue,” <http://glotzerlab.engin.umich.edu/hoomd-blue> (2016).
- [39] J. Towns, T. Cockerill, M. Dahan, I. Foster, K. Gaither, A. Grimshaw, V. Hazlewood, S. Lathrop, D. Lifka, G. D. Peterson, R. Roskies, J. R. Scott, and N. Wilkens-Diehr, *Computing in Science & Engineering* **16**, 62 (2014).
- [40] R. Eppenga and D. Frenkel, *Molecular Physics* **52**, 1303 (1984).
- [41] P. E. Brumby, A. J. Haslam, E. de Miguel, and G. Jackson, *Molecular Physics* **109**, 169 (2011).
- [42] W. Mickel, S. C. Kapfer, G. E. Schroder-Turk, and K. Mecke, *Journal of Chemical Physics* **138**, 44501 (2013).
- [43] D. A. Green, *Bulletin of the Astronomical Society of India* **39**, 289 (2011).
- [44] K. Bagchi, H. C. Andersen, and W. Swope, *Physical Review Letters* **76**, 255 (1996).
- [45] M. Ashby, F. Spaepen, and S. Williams, *Acta Metallurgica* **26**, 1647 (1978).
- [46] D. S. Fisher, B. I. Halperin, and R. Morf, *Physical Review B* **20**, 4692 (1979).
- [47] S. T. Chui, *Physical Review B* **28**, 178 (1983).
- [48] P. F. Damasceno, M. Engel, and S. C. Glotzer, *ACS Nano* **6**, 609 (2012).
- [49] G. van Anders, D. Klotsa, N. K. Ahmed, M. Engel, and S. C. Glotzer, *Proceedings of the National Academy of Sciences* **111**, E4812 (2014).

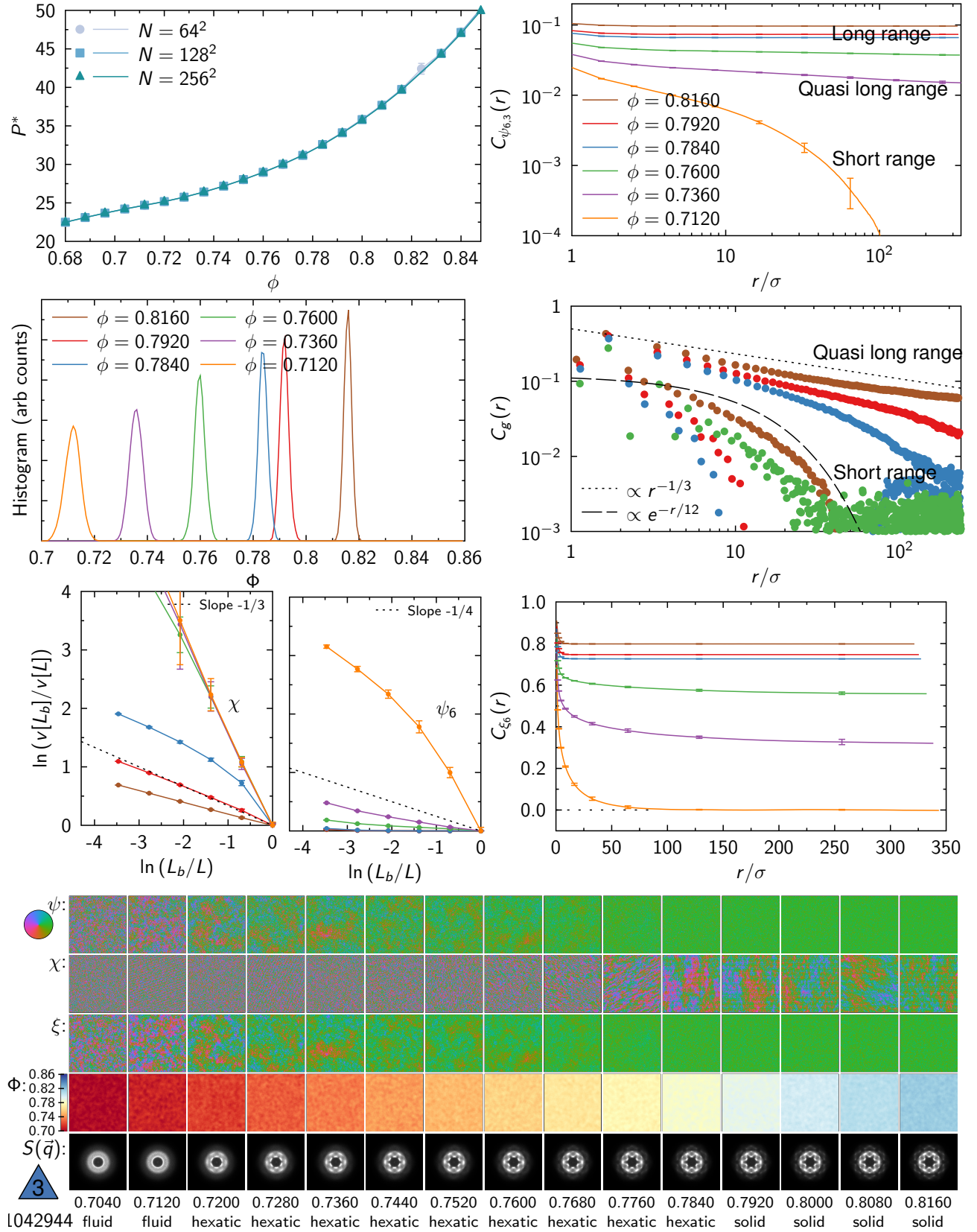


FIG. 9. (top) Triangle equation of state, local density histogram, correlation functions, and sub-block scaling. (bottom) Triangle snapshots. Correlation functions and snapshots computed from  $N = 1042944$  simulations. The double lines in the correlation functions result from the two point unit cell in the honeycomb structure.

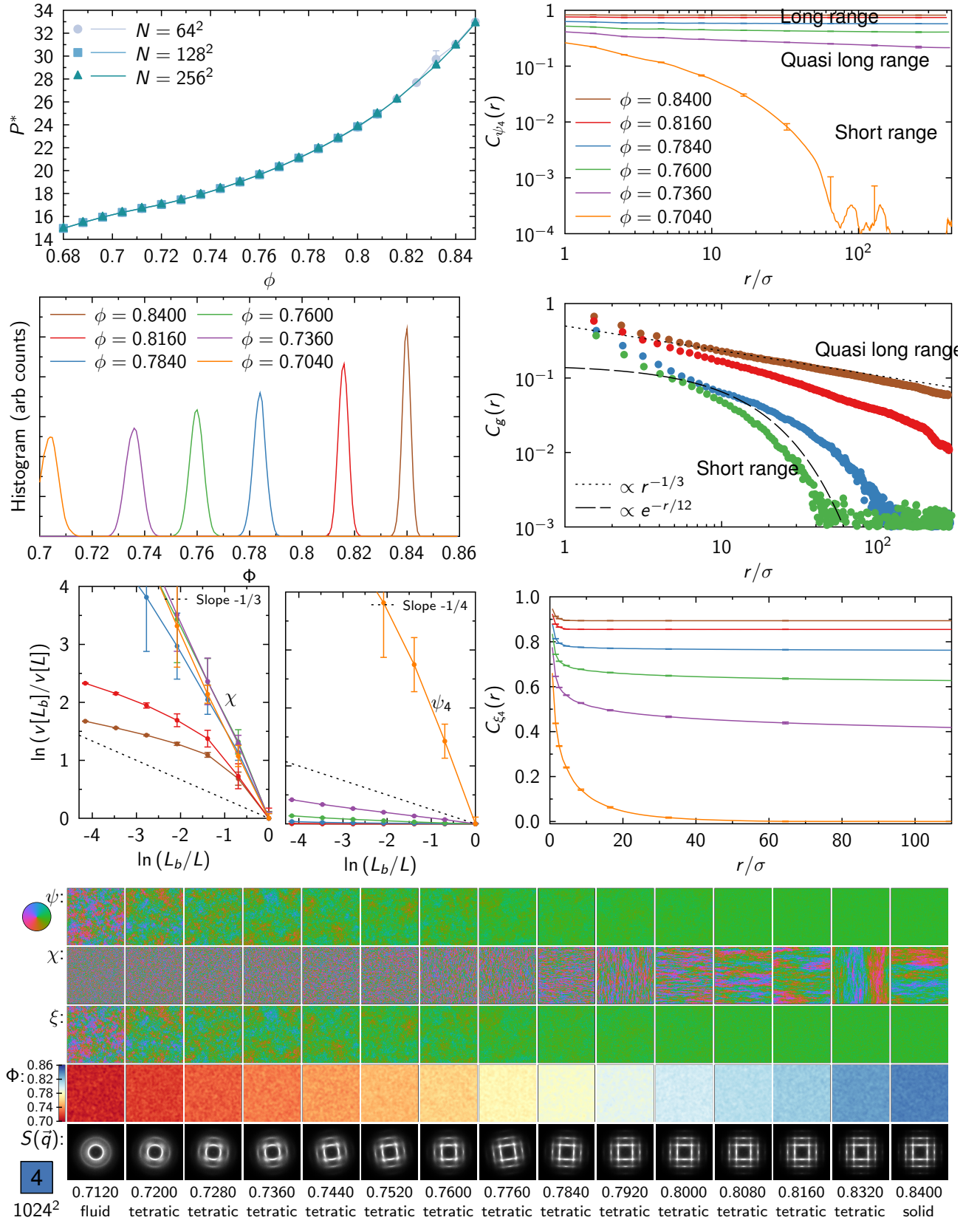


FIG. 10. (top) Square equation of state, local density histogram, correlation functions, and sub-block scaling. (bottom) Square snapshots. Correlation functions and snapshots computed from  $N = 1024^2$  simulations.

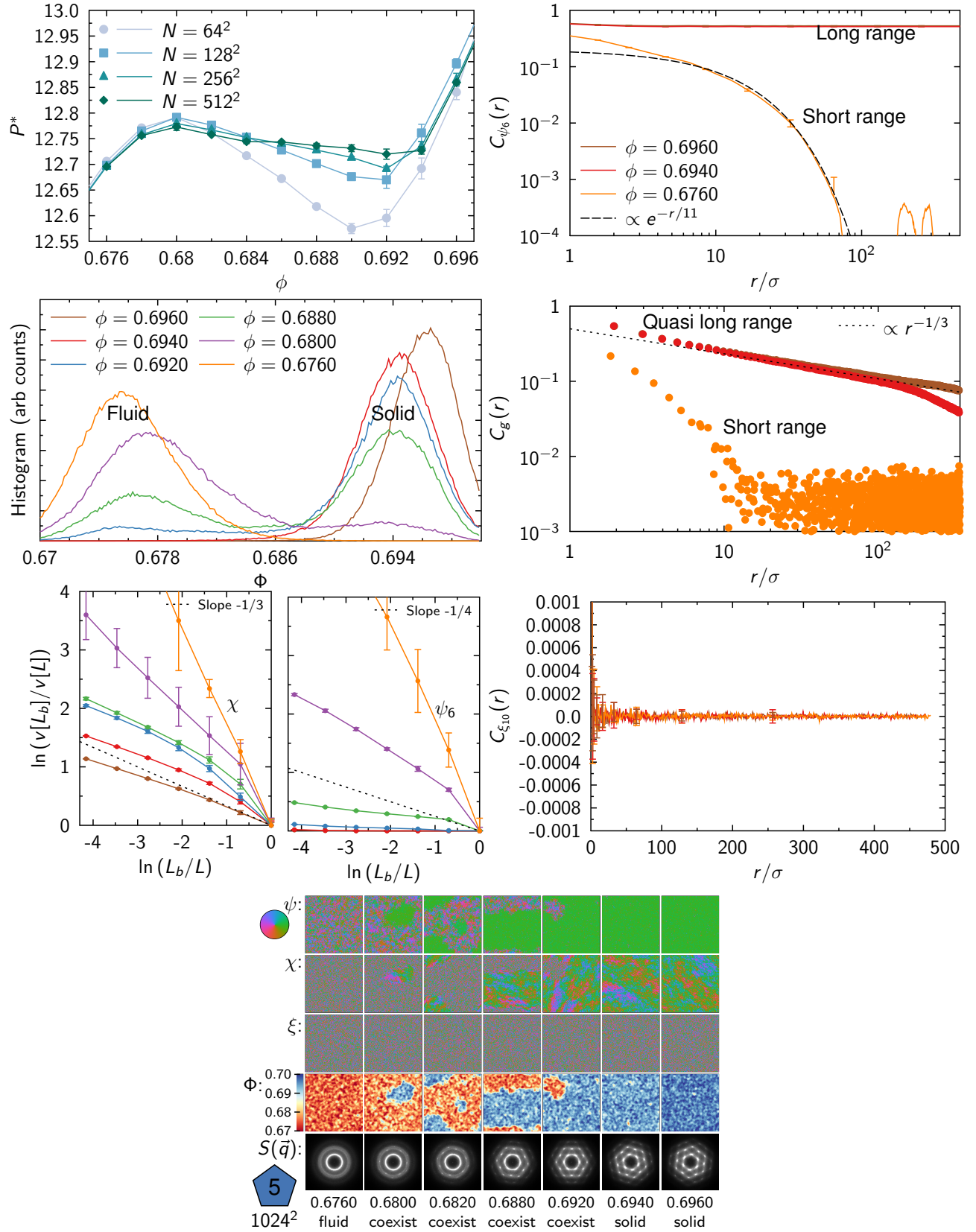


FIG. 11. (top) Pentagon equation of state, local density histogram, correlation functions, and sub-block scaling. (bottom) Pentagon snapshots. Correlation functions and snapshots computed from  $N = 1024^2$  simulations.

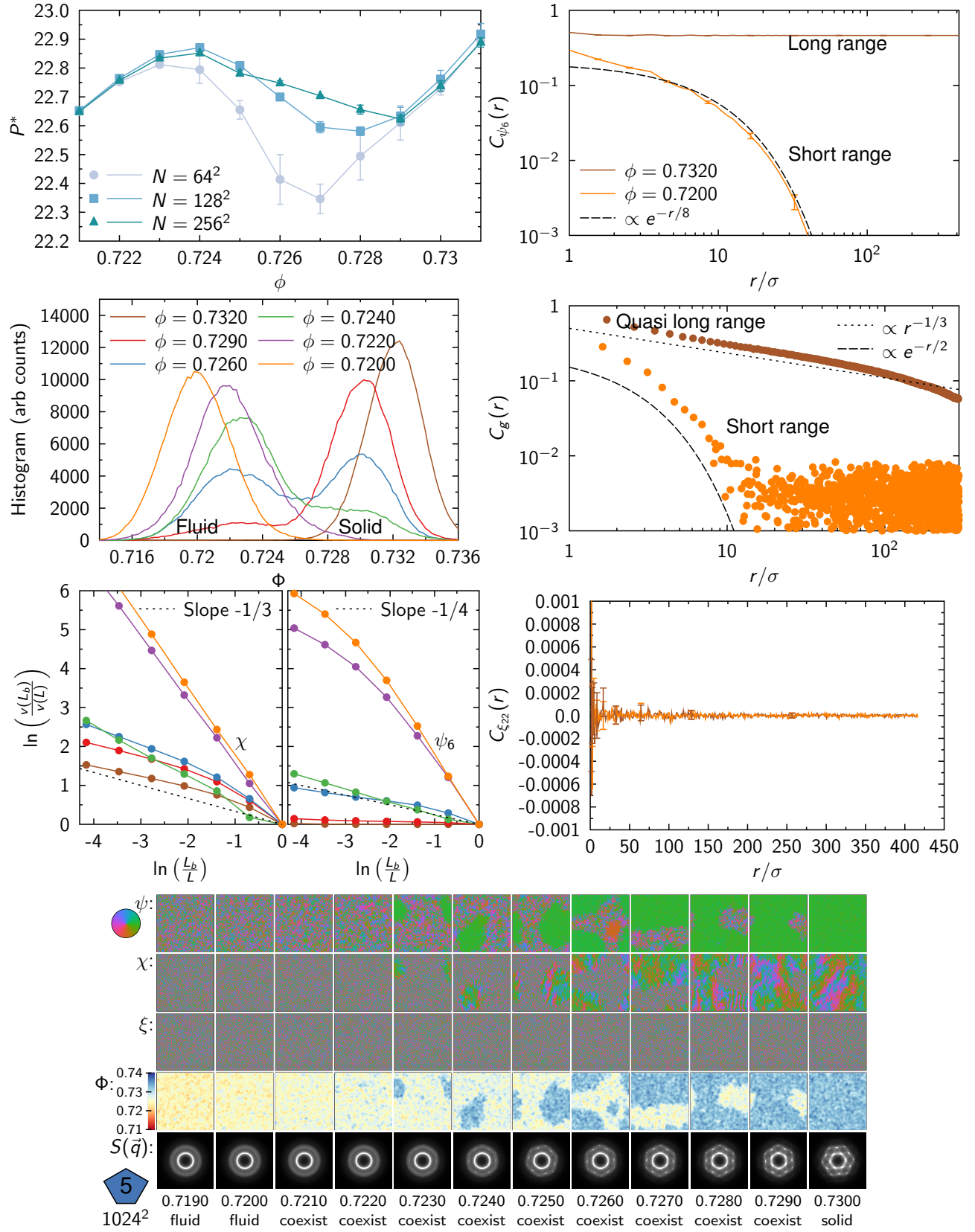


FIG. 12. (top) 4-fold pentile equation of state, local density histogram, correlation functions, and sub-block scaling. (bottom) 4-fold pentile snapshots. Correlation functions and snapshots computed from  $N = 1024^2$  simulations.

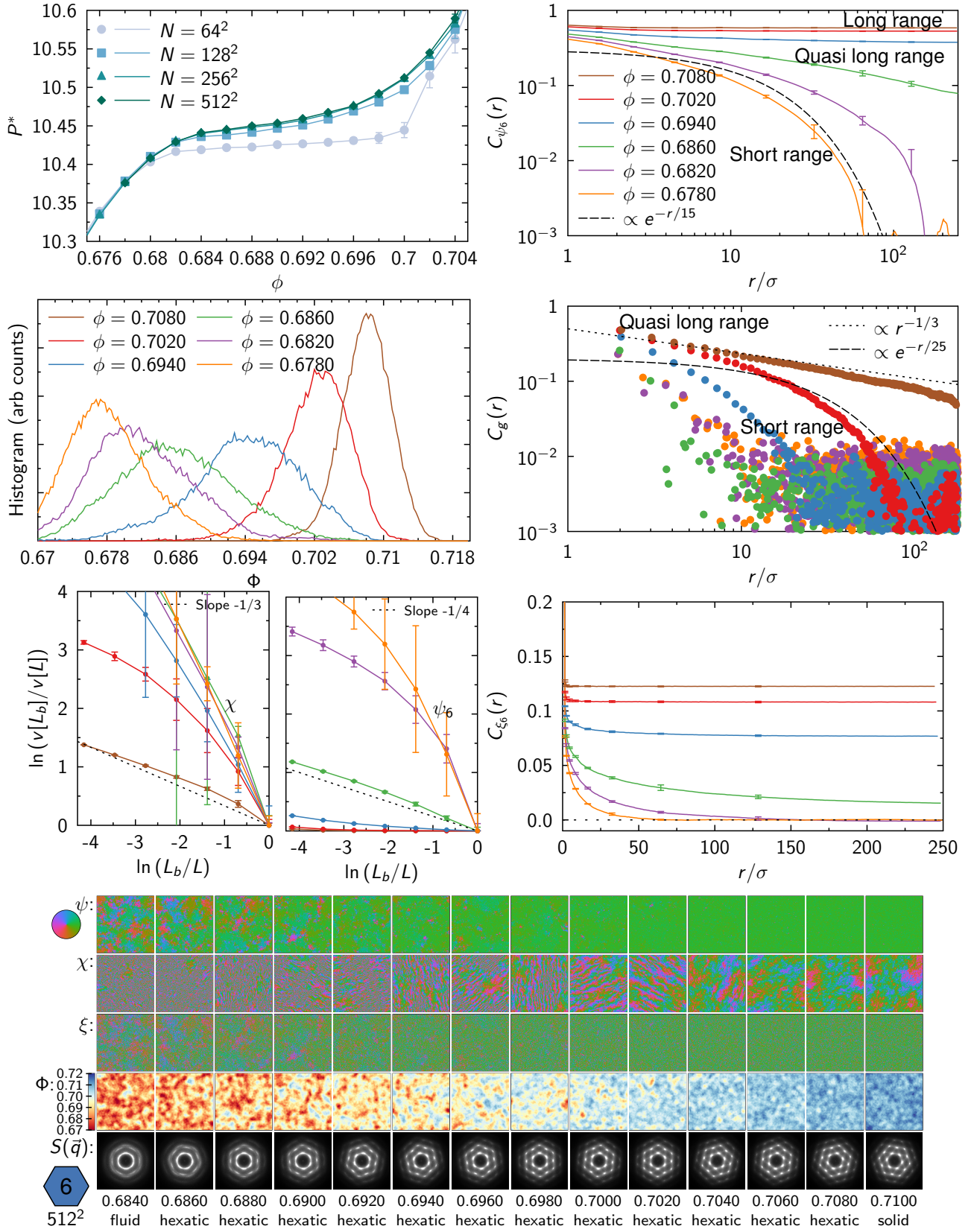


FIG. 13. (top) Hexagon equation of state, local density histogram, correlation functions, and sub-block scaling. (bottom) Hexagon snapshots. Correlation functions and snapshots computed from  $N = 512^2$  simulations.

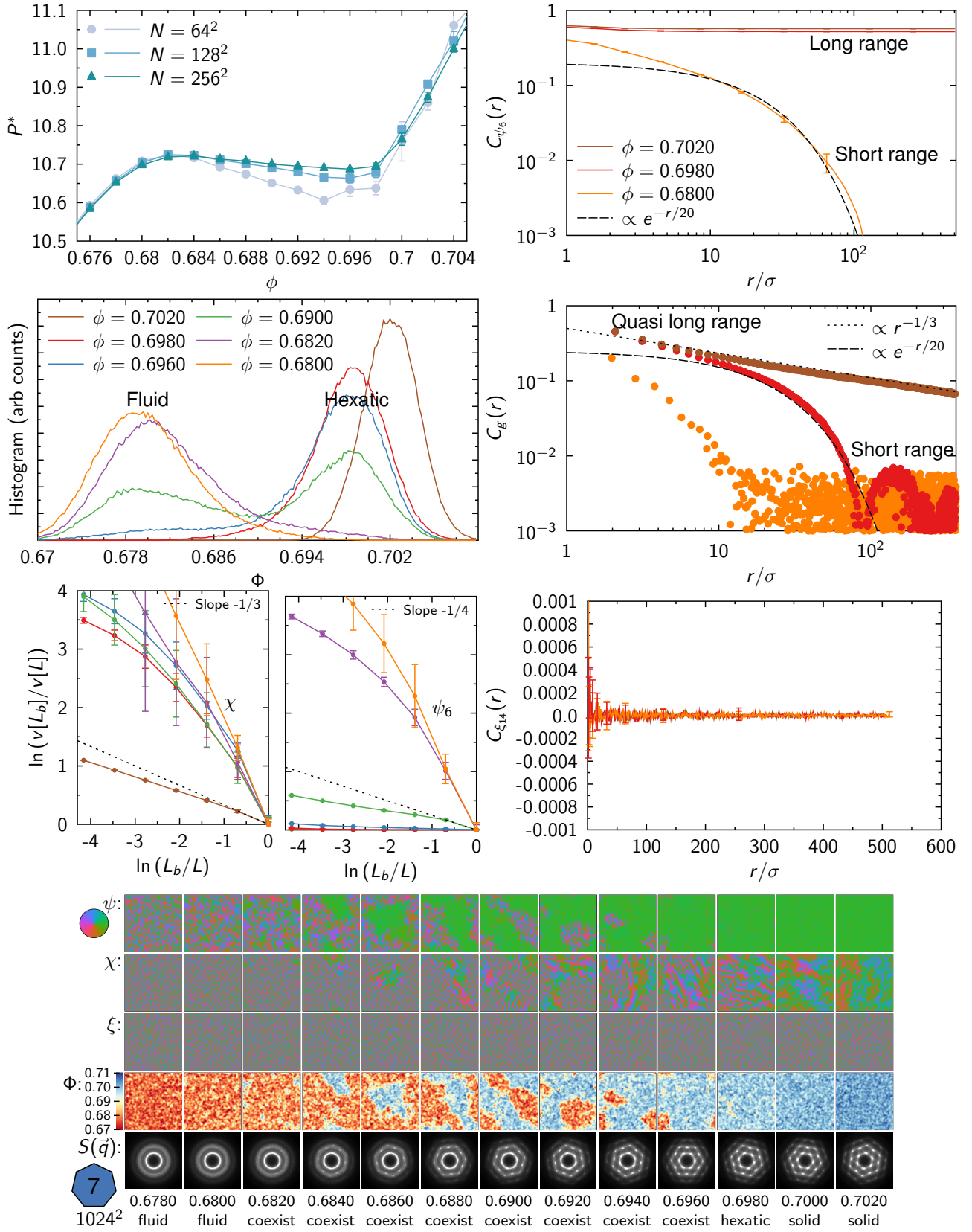


FIG. 14. (top) Heptagon equation of state, local density histogram, correlation functions, and sub-block scaling. (bottom) Heptagon snapshots. Correlation functions and snapshots computed from  $N = 1024^2$  simulations.

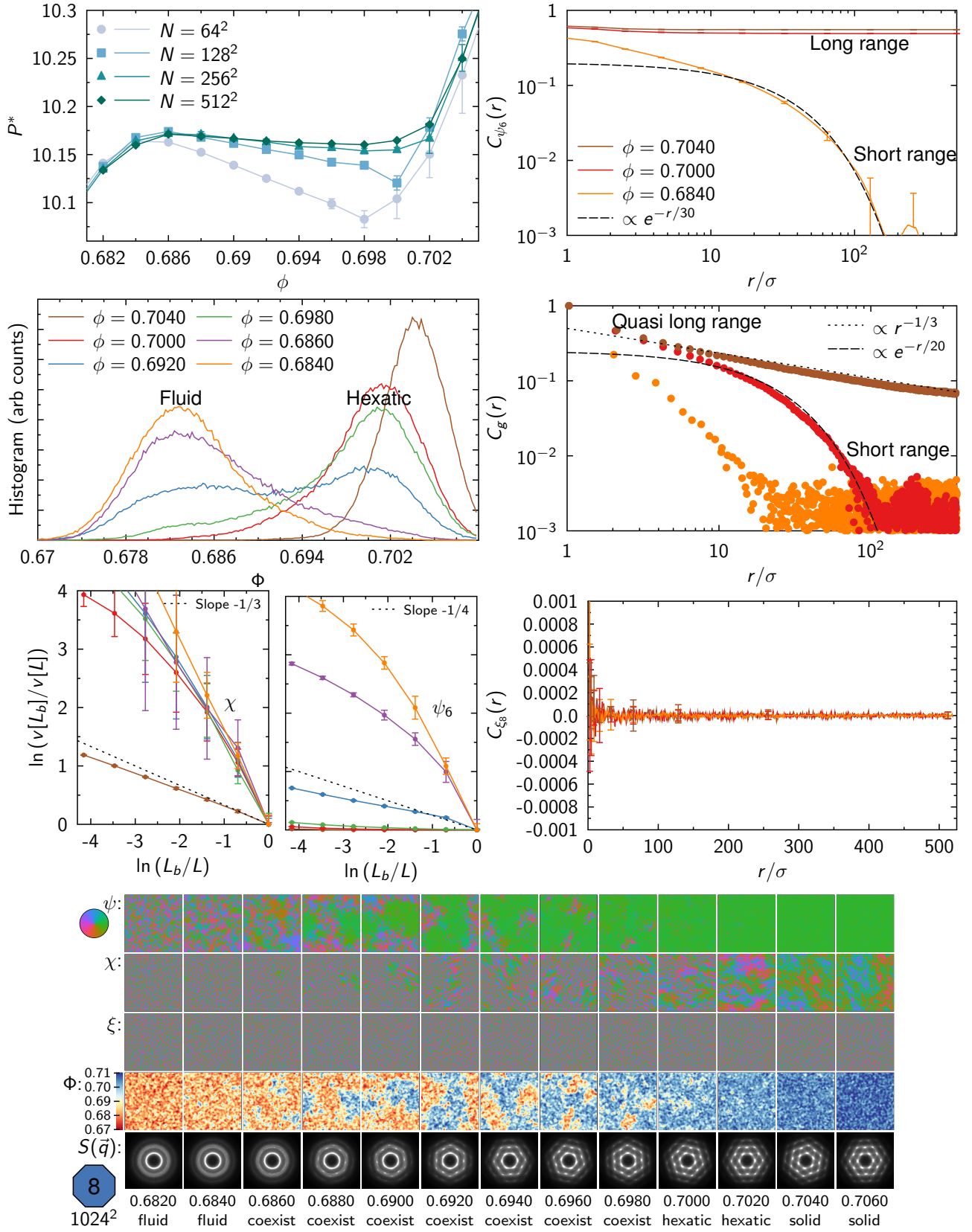


FIG. 15. (top) Octagon equation of state, local density histogram, correlation functions, and sub-block scaling. (bottom) Octagon snapshots. Correlation functions and snapshots computed from  $N = 1024^2$  simulations.

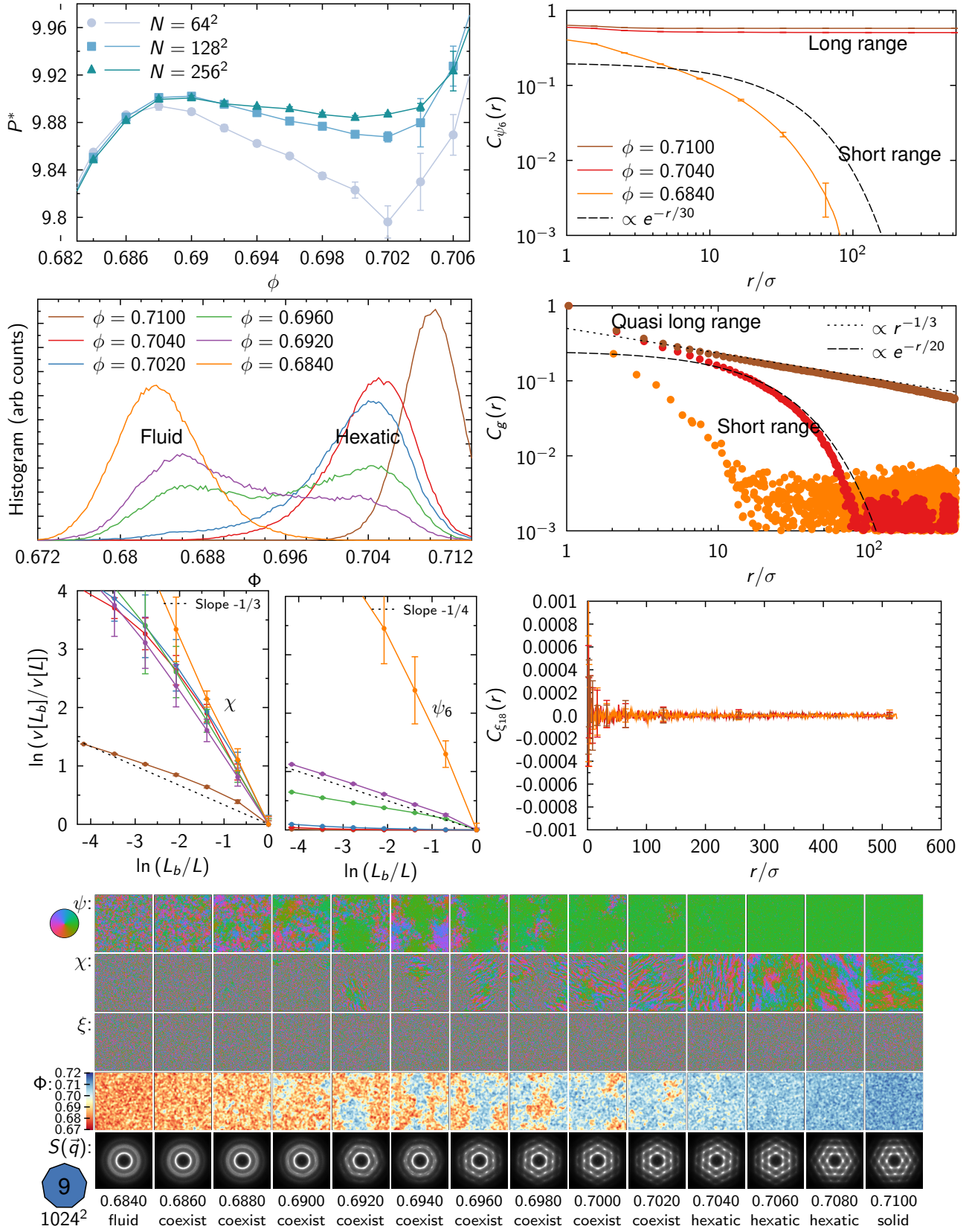


FIG. 16. (top) Nonagon equation of state, local density histogram, correlation functions, and sub-block scaling. (bottom) Nonagon snapshots. Correlation functions and snapshots computed from  $N = 1024^2$  simulations.

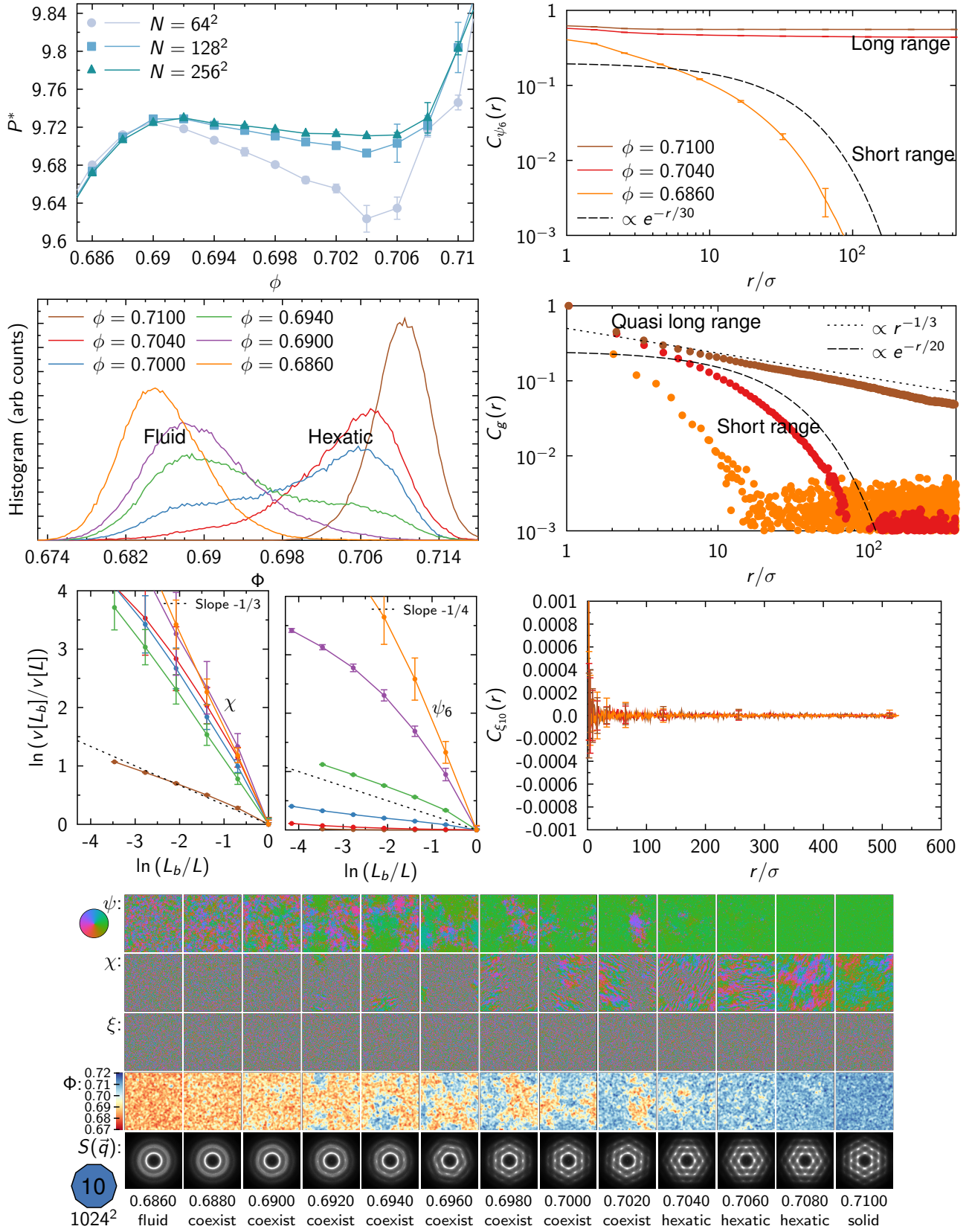


FIG. 17. (top) Decagon equation of state, local density histogram, correlation functions, and sub-block scaling. (bottom) Decagon snapshots. Correlation functions and snapshots computed from  $N = 1024^2$  simulations.

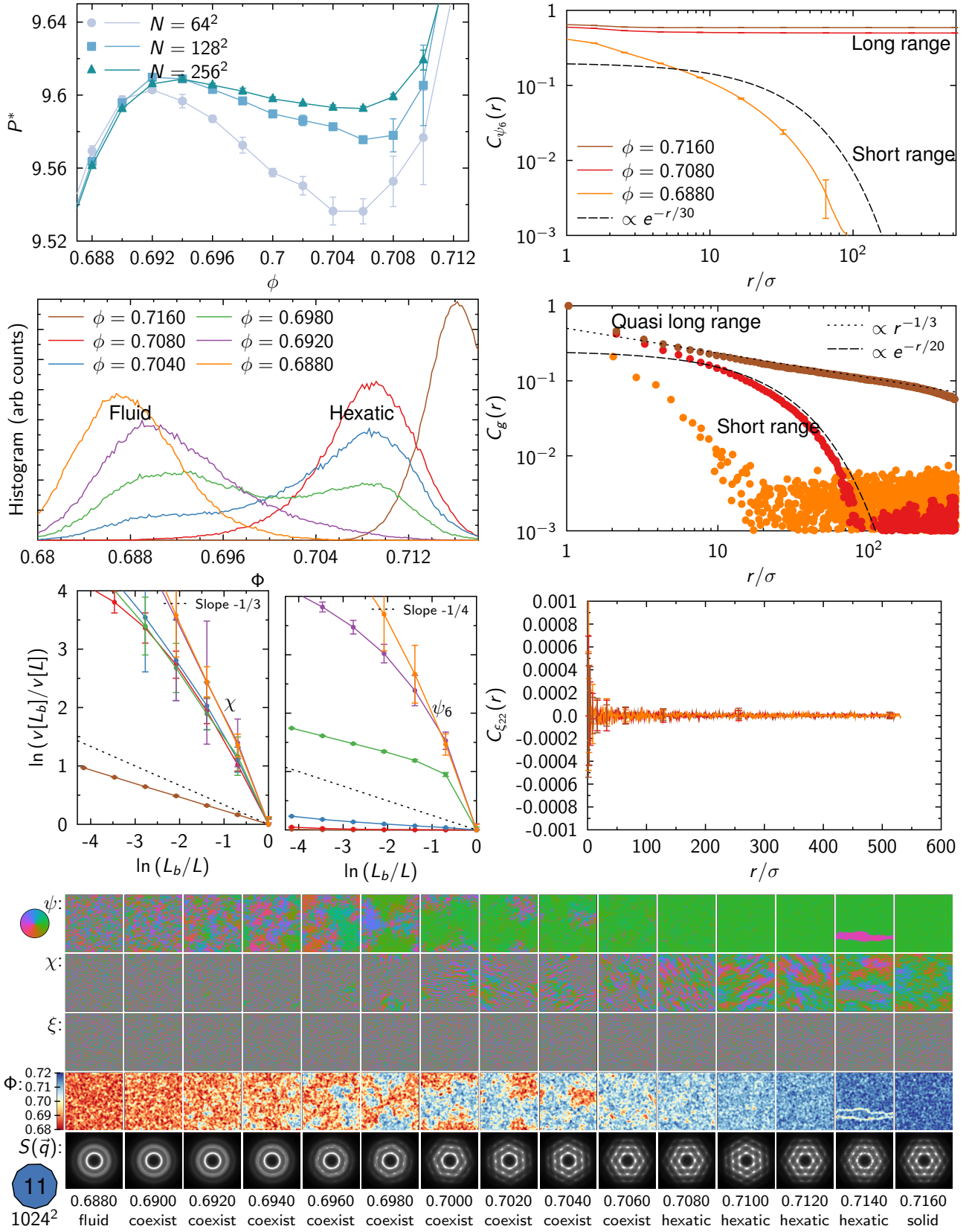


FIG. 18. (top) Hendecagon equation of state, local density histogram, correlation functions, and sub-block scaling. (bottom) Hendecagon snapshots. Note that  $\phi = 0.714$  formed two grains in the simulation. Correlation functions and snapshots computed from  $N = 1024^2$  simulations.

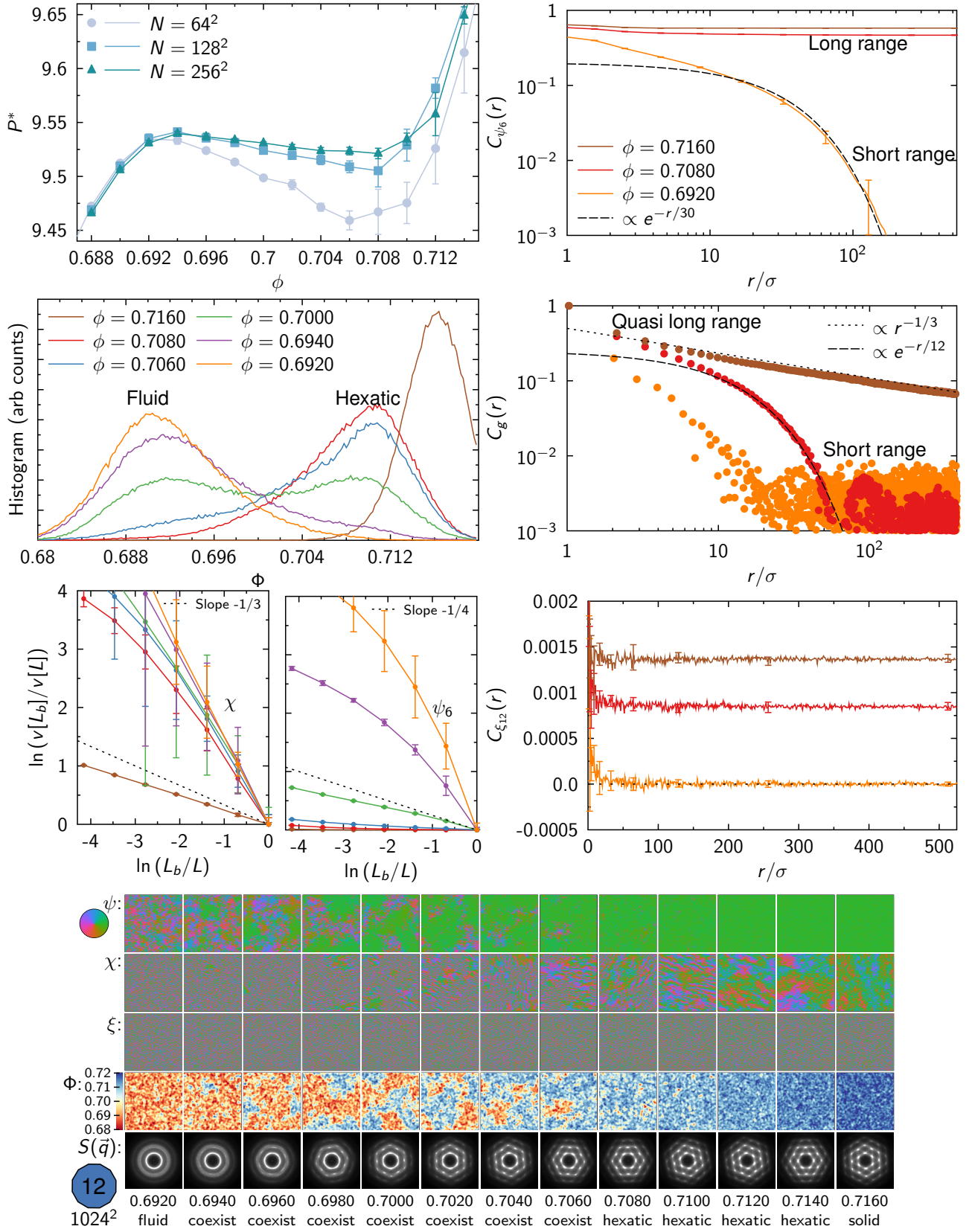


FIG. 19. (top) Dodecagon equation of state, local density histogram, correlation functions, and sub-block scaling. (bottom) Dodecagon snapshots. Correlation functions and snapshots computed from  $N = 1024^2$  simulations.

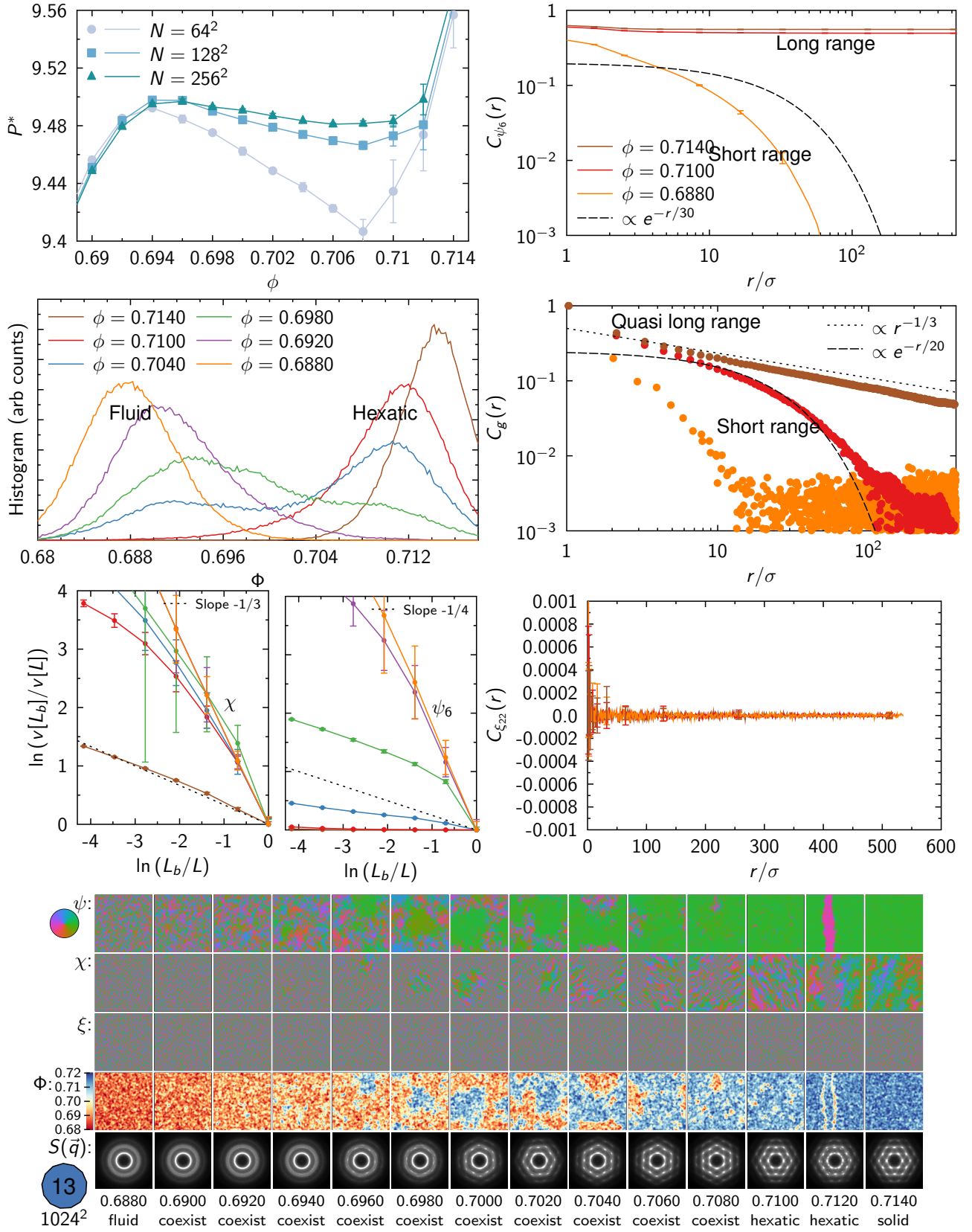


FIG. 20. (top) Tridecagon equation of state, local density histogram, correlation functions, and sub-block scaling. (bottom) Tridecagon snapshots. Note that  $\phi = 0.712$  formed two grains in the simulation. Correlation functions and snapshots computed from  $N = 1024^2$  simulations.

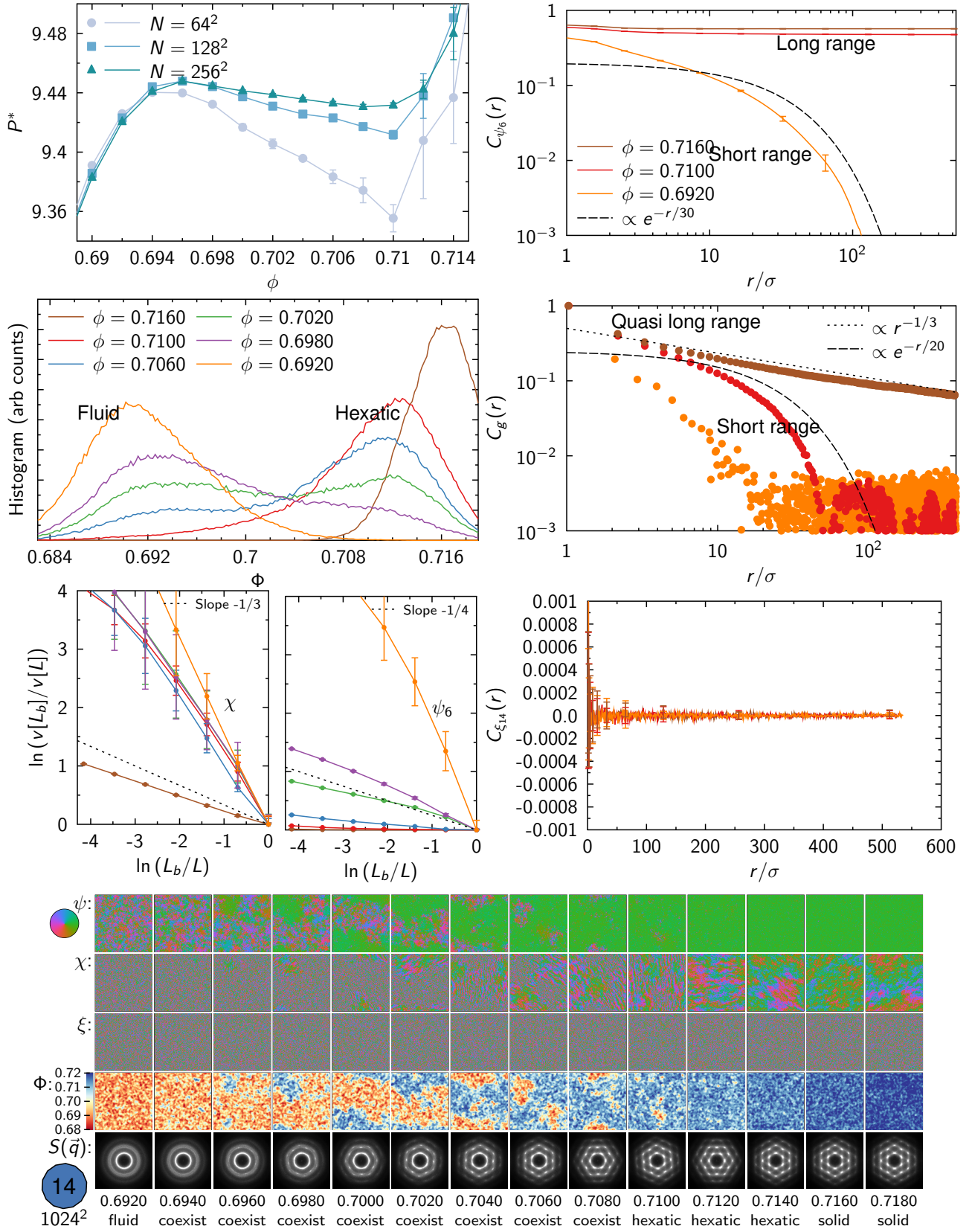


FIG. 21. (top) Tetrads equation of state, local density histogram, correlation functions, and sub-block scaling. (bottom) Tetrads snapshots. Correlation functions and snapshots computed from  $N = 1024^2$  simulations.